

Placeholder Title

Master Thesis

C. Christoforidis



PLACEHOLDER TITLE

MASTER THESIS

by

C. Christoforidis

in partial fulfillment of the requirements for the degree of

Master of Science
in Biomedical Engineering

at the Delft University of Technology.

Student number: 4737822
Project duration: 2018 – 2019
Supervisor: Dr. ir. A.L. Schwab, TU Delft
Thesis committee: Dr. ir. R. Happee, TU Delft
MSc. G. Dialynas, TU Delft

This thesis is confidential and cannot be made public until January, 2020.

©2019

C. Christoforidis

ALL RIGHTS RESERVED An electronic version of this thesis is available at
<http://repository.tudelft.nl/>.

ABSTRACT

*C. Christoforidis
Delft, April 2018*

CONTENTS

1	Introduction	1
2	The effect of haptic feedback in the balance task of bicycling	3
2.1	Abstract	3
2.2	Introduction	3
2.3	Methods	4
2.3.1	Description of experimental set-up	4
2.3.2	Description of steer-by-wire controller	4
2.3.3	Experimental Procedure	5
2.3.4	System Identification	5
2.3.5	Comparison Metrics	6
2.4	Results	7
2.5	Discussion and Conclusions	7
3	Rider control identification in bicycling using gray box approach	11
3.1	Introduction	11
3.2	Methods	12
3.2.1	Bicycle Model	13
3.2.2	Rider Control Model	15
3.2.3	Parameter Estimation	16
3.3	Results	18
3.3.1	Zero Delay Model	18
3.3.2	Variable Delay Model	19
3.3.3	Reafferent Optimal Prediction Model	19
3.4	Discussion	20
3.5	Conclusions	25
A	Calibration of Inertial Measurements	43
B	Orientation Estimation from Inertial Measurements	47
B.1	Offline Estimation Methods	47
B.2	Online Estimation Methods	48
C	Estimation of Rider Torque	53
C.1	Steer rate and acceleration	53
C.2	Steering shaft moment of inertia and viscous friction	53
C.3	Motor Torque Input Validation	56
C.3.1	Design of torque sensor	56
C.3.2	Results	57
Bibliography		61

1

INTRODUCTION

Bicycle riding is a fundamental part of everyday transportation in many countries around the world. Ever since the development of the safety bicycle(two equal sized wheels, pneumatic tires, chain drive, rear wheel propulsion and a bent front fork), almost 130 years ago, the bicycle remains one of the most prominent means of transport [17]. With the growing concerns of sedentary lifestyles many choose the bicycle as their primary commute vehicle with the hopes of maintaining some levels of fitness. Additionally the bicycle is the preferred means of physical exercise for the elderly especially in the Netherlands and Denmark. Despite the fact that riding a bicycle is an acquired skill that we learn from our early childhood and we use throughout our life, the fundamental laws of human bicycle control are not yet understood.

According to the European Road Safety Observatory [2] in 2016 about 2.000 cyclists were killed in road accidents throughout the EU. Despite the overall reduction in the road toll (down 40% from 2007), the proportion of cycling related fatalities increased, from 6% in 2007 to 8% in 2016 [2]. In a recent study examining the entries of patients to the emergency department due to traffic related accidents in the Netherlands (see Fig. C.3), it was found that cycling accidents were the most prevalent. With over 60,000 reported cases bicycle accidents outnumber automobile accidents more than 4 to 1. It therefore becomes clear that a lot could be done to improve cycling safety. Further look at the figure will reveal that most of those accidents did not involve a second party. In these cases the rider just fell off his bike. Although there are several potential reasons that riders lose control of the bicycle, formulating a general model of how humans control single track vehicles could prove invaluable in understanding the causes behind the above numbers.

Following the steps of early cybernetics research in which airplane pilot modeling was pioneered by McRuer[22–24], a plethora of authors attempted adapting McRuers crossover model in order to model the rider of a seemingly much more complex task; motorcycle and bicycle riding. However, some argued that such an approach will not work since cycling is not just a compensatory task. Moreover little concern was made to the fact that humans try to optimize for performance while simultaneously exerting the lowest amount of control effort. These spawned a new wave of research focusing in optimal control. This approach is based in early motor control research in which the human brain is believed to work as a constrained optimal controller.

A further look in motor control research reveals the importance of the internal model in control, state estimation and dead time compensation [9, 10, 12, 41]. The internal model theory argues that the motor system is controlled by the constant interactions between the process and the controller. In this case the process is the body, however in tasks like cycling the bicycle can be considered as an extension of the body. The internal model can be used either as a tool for control in the form of the inverse model [8, 11] or as a forward model in state estimation in combination with Kalman filters [41]. Additionally, forward models can be used in delay compensation algorithms [26, 37].

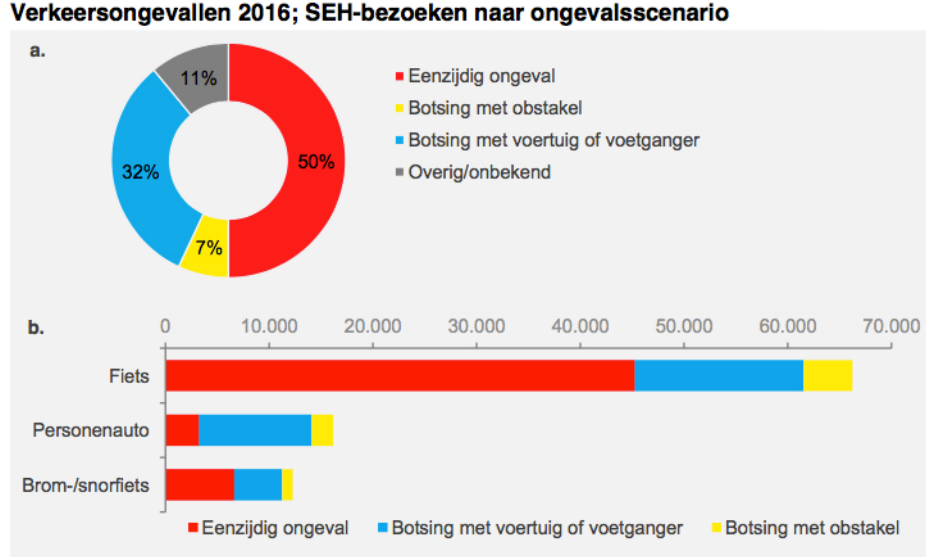


Figure 1.1: The number of road users that visit the emergency department at a hospital after a traffic accident in the Netherlands in 2016. Red indicates single vehicle accidents, yellow indicates a collision with an obstacle, blue indicates multi-vehicle accident and grey indicates other type of accidents[19].

In this work an attempt to iterate over existing rider control models is made with the goal of answering two important questions.

- How significant is the effect of torque feedback for the balance task of bicycling?
- What is the prediction strategy best suitable for dead time compensation in the balance task of bicycling?

In order to answer the above questions system identification techniques are employed using the experimental dataset acquired within the scope of this thesis. In chapter 2 an attempt is made to investigate the effect of haptic feedback in the task of balancing a bicycle under lateral perturbations. Non-parametric identification was conducted on the response of 20 riders in two different experimental conditions. In the first one the experimental bicycle operated as a normal bike while in the second the coupling between roll and steer was modified in order to cancel the torque feedback that would naturally transfer from the front wheel contact point to the handlebars. In chapter 3 further analysis is conducted by applying gray box identification techniques in order to investigate again the importance of torque feedback but also to test the effect of time delays in sensory feedback pathways and how these can be compensated through the use of internal model theory. In appendices A to C further details are presented on the methodology used to acquire proper measurements from the sensors of the experimental platform.

2

THE EFFECT OF HAPTIC FEEDBACK IN THE BALANCE TASK OF BICYCLING

¹Corresponding article: G. Dialynas, C. Christoforidis, R. Happee, A. L. Schwab, The effect of haptic feedback in the balance task of bicycling, In Proceedings of the 4th Triannual International Bicycle and Motorcycle Dynamics Conference (2019).

2.1. ABSTRACT

The objective of this research is to study the effect of haptic steering feedback on the balancing task of a bicycle during lateral perturbation tests, in an effort to improve two-wheeler safety. The steer-by-wire bicycle designed and built at TU Delft bicycle laboratory is used as an experimental platform to analyze the rider response with and without steering feedback. The response of the rider's control actions is represented in the time domain by means of impulse response functions (IRFs). More specifically, three metrics are defined in order to assess both steering and balancing performance. Results failed to indicate any statistically significant difference between experimental conditions. Although, it should be mentioned that parametric rider control identification of the sensory systems might be prerequisite to indicate any possible changes.

2.2. INTRODUCTION

Since the birth of the safety bicycle in the 1890s, dynamics and self-stability have been subjects of numerous discussions and bodies of research. These issues can nowadays be considered to be partly resolved [18] for a wide range of applications. Still, the question remains on how the rider stabilizes the lateral motions of the bicycle when it's driven at low (unstable) forward speeds or how the rider follows a desired path; e.g. the required control inputs and the rider learning process. These probably comprise of haptic, vestibular and visual cues; here we will focus on the haptic cues and the task of stabilization.

Haptic systems in vehicle control are usually connected with two types of realities. One current application of kinesthetic devices is focused on enabling the driver to feel feedback from the vehicle state when steer-by-wire systems come into play. Steer-by-wire vehicles often need a resistance torque to prevent excessive rotation of the steering wheel. This feedback torque is often defined by a simple relation, e.g. a function of wheel angle, wheel torque, or vehicle state, and aims to assist the driver in achieving the desired trajectory in real performance [14]. Similarly, haptics can also be used as a tool to improve first stages of task learning through fading guidance towards a goal [3]. On the other hand, computer simulations can be helpful in evaluating different strategies for steering control [20], as a previous stage to its implementation, and in development of control systems aimed to improve riding safety [21].

In this work we use the experimental steer-by-wire bicycle [6] which has been developed in the TU Delft bicycle laboratory to study the effect of haptic feedback in the balancing task of bicycling. This is achieved by analyzing the rider response with and without steering feedback during lateral perturbation tests. The response of the rider's control actions is represented in time domain by means of impulse response functions

(IRFs). More specific, the applied steer angle and the estimated roll angle is used as a measure of control effort and performance respectively.

The paper is organized as follows: After this brief introduction the experimental set-up and experimental procedure are presented. Next, the methods followed by the results are described. The article ends with the discussion and conclusion section providing further insights in an attempt to explain the findings of this research.

2.3. METHODS

2.3.1. DESCRIPTION OF EXPERIMENTAL SET-UP

At TU Delft an instrumented steer-by-wire bicycle which is fully equipped with a number of sensors to measure the state and rider input has been designed and build, see figure 2.1. For this study measurements from the inertial measurement unit (IMU) sensor (MPU-9250) and the steering angle encoder (RMB-20SC) are used. In addition, a perturbator mechanism is present, which is used to excite the system. These perturbations are applied by laterally pulling a rope with a force transducer in series, which is attached on the seat post. All sensors output are logged with a sampling frequency (F_s) equal to 1000 Hz. The measurement bicycle is electrically driven and has a cruise control system, so the rider does not need to exert pedaling power and thus eliminates the need for lower limb movement. Steering angle (δ) is directly measured from the absolute encoder of the upper front assembly, while the roll angle (ϕ) is estimated from the IMU data using the approach described by Sanjurjo et al. [32].



Figure 2.1: Prototype of the steer-by-wire bicycle with steering and handlebar actuators, sensors, digital controller and custom made battery pack.

2.3.2. DESCRIPTION OF STEER-BY-WIRE CONTROLLER

To minimize the difference between the handlebar angle θ and the fork angle δ , tracking control has been implemented. In this way, the steer-by-wire system should behave like an ordinary, mechanically steered bicycle, when the rider applies a steer torque at the handlebar. Two proportional-differential PD-controllers are implemented in order to provide an action-reaction torque T_{PDH} to the handlebar and T_{PDF} to the fork assembly. Angular velocity $\dot{\theta}$ and $\dot{\delta}$ are estimated by taking the time derivative of angular position θ and δ respectively, for a fixed time interval of 1 ms. The double PD-configuration can also be used to manipulate the steer feedback torque independent of the tracking performance. The double PD-controller is of the following

form:

$$T_{PDF} = K_{PF}(\theta - \delta) + K_{DF}(\dot{\theta} - \dot{\delta}), \quad (2.1)$$

$$T_{PDH} = K_{PH}(\theta - \delta) + K_{DH}(\dot{\theta} - \dot{\delta}) \quad (2.2)$$

with proportional gains K_{PH} , K_{PF} and differential gains K_{DH} , K_{DF} respectively. The torque T_{PDH} is applied at the upper servomotor, and the torque T_{PDF} at the lower servomotor. By setting T_{PDH} to zero a steering configuration is created where the rider feels no reaction torque from the steering assembly (feedback "off"), without majorly affecting tracking error performance. The current controller configuration performs with high level of accuracy up to 3 Hz, the tracking error is kept below 3 degrees. However, in certain conditions non-linear effects of the servomotors and tires might create a delay in the control loop effecting the tracking error and realism of the haptic steering feel.

2.3.3. EXPERIMENTAL PROCEDURE

Twenty healthy subjects volunteered in this study. To assure safety all subjects were requested to wear protective equipment in the shape of a standards-approved bike helmet, knee and elbow pads. All participants gave informed consent according to the guidelines of the human research ethics committee of Delft University of Technology. All subjects were healthy and reported that they did not experience any kind of pain or injury in the year before the experiments. The mean weight of all subjects was selected to be close to the European population [39].

Each experiment trial consisted of four different speeds (i.e., 2.6, 3.7, 4.5, 5.6 m/s). Two individual trials were performed in total for every speed. In the first trial steering feedback was enabled, whereas in the second trial steering feedback was disabled. Every trial had a duration of approximately 60 seconds. All experiments were performed across Heertjeslaan cycling path of TU Delft, the subjects were requested to ride the steer-by-wire bicycle in all aforementioned speeds while being laterally perturbed. An additional bicycle was used from the experiment coordinator to cycle next to the instrumented steer-by-wire bicycle and perturb the subject, see figure 2.2. A set-up which allowed both push and pulls was initially tested but the pushes were subject to inconsistencies. After inspecting the data of the pilot runs, it was observed that unilateral disturbances did not affect the predictability of the perturbation, as the response of the rider was similar. For this reason the unilateral approach was chosen. Nevertheless, to avoid any feedforward control behaviour (e.g., seeing the coordinator preparing to pull the rope) all subjects were asked to keep their focus on the road ahead.

2.3.4. SYSTEM IDENTIFICATION

In order to remove the effects of unwanted disturbances and noise, the measured steering angle and estimated roll angle signals were filtered through a finite impulse response (FIR) model. The impulse response function is defined as the function $h(\tau)$ which when convoluted with external input $w(t)$ results in the output $y(t)$. The output data either represents $y(t) = \phi(t)$ corresponding to $h_\phi(\tau)$ or $y(t) = \delta(t)$ corresponding to $h_\delta(\tau)$. In discrete time the convolution can be approximated by the following equation:

$$y(t) = \sum_{\tau=0}^{T-1} h(\tau) w(t-\tau) \Delta\tau + v(t) \quad (2.3)$$

where T is the time length of the impulse function, which is equal to 3.08 seconds as the oscillations die out after that point and $v(t)$ the remnant which is caused by unwanted disturbances. Equation C.2 is rewritten in matrix form as follows:

$$y = Wh + v \quad (2.4)$$

where W is the matrix containing time shifted versions of the input signal.

$$W = \begin{bmatrix} w(0) & 0 & 0 & \dots & 0 \\ w(1) & w(0) & 0 & \dots & 0 \\ w(2) & w(1) & w(0) & \dots & 0 \\ \vdots & \vdots & \vdots & \ddots & 0 \\ w(N-1) & w(N-2) & w(N-3) & \dots & w(N-T) \end{bmatrix} \quad (2.5)$$



Figure 2.2: Experimental trial performed across Heertjeslaan cycling path of TU Delft; Experiment coordinator cycling next to steer-by-wire bicycle while pulling laterally the subject with a rope.

Since equation 2.4 is linear in the parameters (the coefficients of h) there exists a unique solution that can be found through the least squares method.

$$\hat{h} = (W^T W)^{-1} W^T y \quad (2.6)$$

Having an estimate of the IRE, the input signal is convoluted with (\hat{h}) in order to produce an estimate of the output (\hat{y}) without the noise. The estimated responses are further smoothed using a eight-order Butterworth filter with cutoff frequency of 10 Hz.

2.3.5. COMPARISON METRICS

In order to correctly assess if there is a statistically significant difference between the two conditions, three metrics are defined. The first one is the Power Spectral Centroid (PSC) of measured angle (δ) defined as

$$(PSC_x, PSC_y) = \left(\frac{\sum_{n=1}^N f(n) S_\delta(n)}{\sum_{n=1}^N S_\delta(n)}, \frac{\sum_{n=1}^N S_\delta(n)^2}{\sum_{n=1}^N S_\delta(n)} \right) \quad (2.7)$$

where N is the number of samples lower than 5 Hz and $S_\delta(f)$ the power spectral density of the signal. This metric gives an indication of the frequency which most of the power in the signal is centered around. Higher value of PSC_x will indicate more oscillatory behaviour for the steering response and can be used as a metric of control effort.

The variance accounted for (VAF) is used to assess the quality of the fit of the FIR model output. The runs which scored lower than 60% were removed from further analysis as it was deemed that the model did not sufficiently capture the characteristics of the raw signal. The VAF between \hat{h}_ϕ^{off} and \hat{h}_ϕ^{on} is also used as a metric of similarity for the roll angle response. In that case VAF is defined as :

$$VAF_\phi = \left(1 - \frac{\text{var}(\hat{h}_\phi^{off} - \hat{h}_\phi^{on})}{\text{var}(\hat{h}_\phi^{off})} \right) \cdot 100\% \quad (2.8)$$

Finally as a third test, the relative delay between the steering angle IRFs of the two conditions is estimated by finding the lag value of maximum cross-correlation between the signals.

2.4. RESULTS

An independent 2-sample t-test was conducted to compare if there was significant difference (95 % confidence interval) in steering effort between conditions for all speed levels, see figure 2.3. For the low speed level (2.6 m/s) there was no significant difference in PSC_x for "feedback on" ($M = 0.79$, $SD = 0.08$) and "feedback off" ($M = 0.76$, $SD = 0.10$) conditions; $t(38)=1.00$, $p=0.3222$. For speed 3.7 m/s there was again no significant difference in the metric for "feedback on" ($M = 0.92$, $SD = 0.11$) and "feedback off" ($M = 0.92$, $SD = 0.11$); $t(38) = -1.03$, $p=0.3075$. For 4.5 m/s there was also no significant difference in the scores for "feedback on" ($M = 0.98$, $SD = 0.14$) and "feedback off" ($M = 0.98$, $SD = 0.14$); $t(38) = -1.04$, $p=0.3062$. And finally, for 5.6 m/s no significant difference was found in the PSC_x for "feedback on" ($M = 1.1$, $SD = 0.16$) and "feedback off" ($M = 1.1$, $SD = 0.16$) conditions; $t(38) = -1.6$, $p=0.118$.

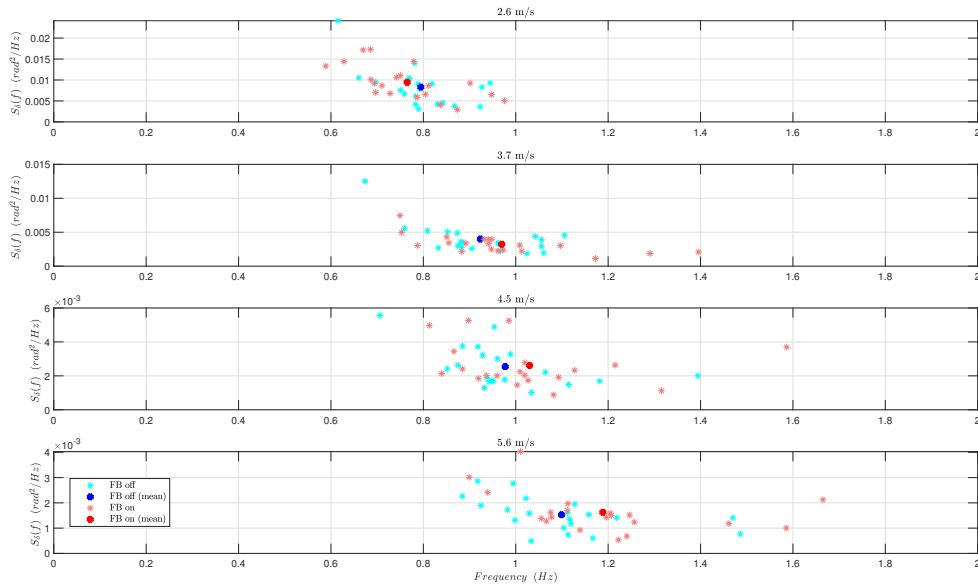


Figure 2.3: The x and y coordinate of the PSC used to determine the frequency where most of the power is concentrated.

The impulse response function of the mean rider for steer angle (δ) and roll angle (ϕ) is shown in figure 2.4. The variance accounted for between roll angle impulse responses (see equation 2.8) is averaged over all participants and displayed for all speed levels in figure 2.5 (a). Similar roll angle response between "feedback on" and off indicated by higher VAF_ϕ values suggests matching task performance.

In addition to the variance roll test an one-sample t-test was conducted to examine if there is any delay in the steering response between feedback on and off, see figure 2.5 (b). For 2.6 m/s there was no significant deviation in the delay ($M = -3$, $SD = 25.89$) from zero mean; $t(19) = -0.52$, $p=0.6103$. However, for 3.7 m/s the delay ($M = -20.65$, $SD = 25.93$) was statistically significant; $t(19) = -3.56$, $p=0.0021$. Also for 4.5 m/s the mean of the delay ($M = -23.5$, $SD = 20.88$) was also significantly different than zero; $t(19) = -5.03$, $p=0.0001$. Lastly, for 5.6 m/s there was again significant difference in the delay ($M = -19.15$, $SD = 18.19$) from zero; $t(19) = -4.71$, $p=0.0002$.

2.5. DISCUSSION AND CONCLUSIONS

From the aforementioned results it is suggested that the effects of haptic feedback are minimal to non-existent for the roll stabilization task. Neither performance (see figure 2.5 (a)) or steering effort was affected by the removal of haptic steering feedback. Balance performance among conditions was comparatively consistent (see figure 2.5 (a)). However, in the unstable speed region the variance and the number of outliers were higher. For steering effort the null hypothesis that the PSC_x metric came from independent random samples with equal means and equal variances failed to be rejected for all speed levels. This does not undoubtedly prove that the samples came from the same population, howbeit it gives a strong indication towards that fact. On the other hand, for the "feedback on" the steering response was delayed (≈ 18 ms see figure 2.5 (b)) in

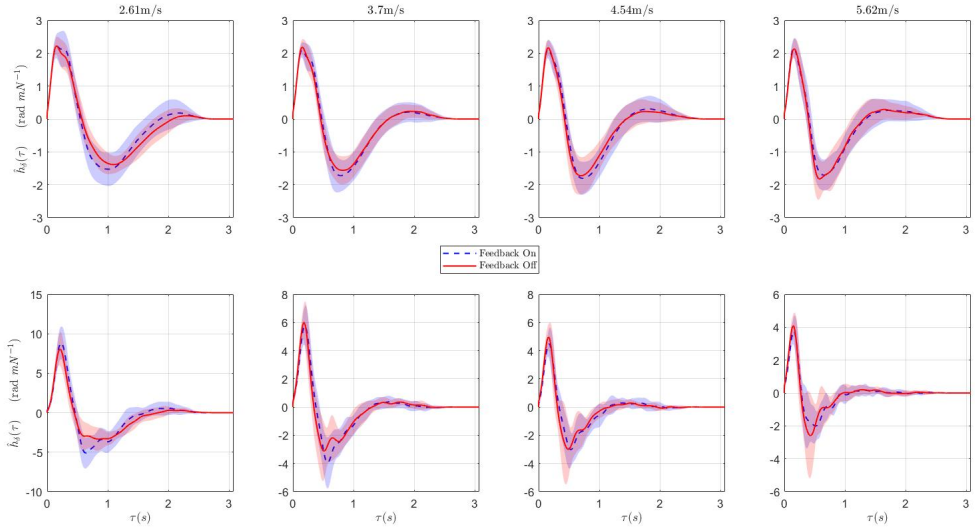


Figure 2.4: The impulse response function of the mean rider for steer angle (δ) and roll angle (ϕ). The shaded area represents the values within one standard deviation of the mean.

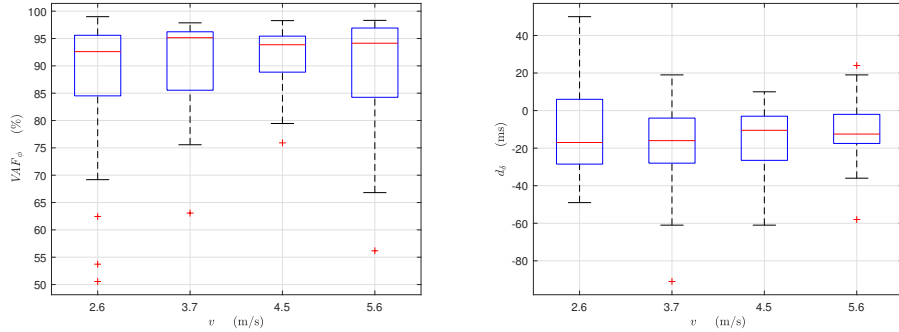


Figure 2.5: a) Box plot of variance accounted for between roll angle impulse response functions for all speed levels. b) Box plot of the relative delay in the estimated steering angle response between the two experimental conditions. Negative value means that the "feedback on" signal is delayed compared to the "feedback off".

comparison to the "feedback off". This might be due to the fact that the handlebars are more inert due to the additional steering feedback.

The lateral pull disturbances can be translated into a lean torque in the direction of forward speed and a steer torque in the direction of the steering axis. This means that any dynamic effects that influences these torques must be examined. The performance of the steer-by-wire controller was examined by numerical simulation and subjective measurements. All subjects reported that they felt like riding a mechanically steered bicycle, no adaptation period was required before the experiments. During the experiments very little motion of the upper body was evident and steer control was expected to be the main mechanism for bicycle balance [27]. Thus, we assume that the intrinsic and reflexive responses of the upperbody do not affect the validity of these results.

Physiologically there are two ways in which proprioception works in order to give the rider information regarding the state of the front assembly. First are the muscle spindles which by detecting changes in velocity and position of the shoulder joint give the rider an estimation of the steering angle and steering rate of the handlebars. Second are the Golgi tendon organs which work as force feedback sensors. The sensory information provided by the latter sensor is what this experiment tried to invalidate. In the feedback on case, information from the ground reaction torque of the front tire is transferred through the handlebars to the sensory receptors of the rider arms and is used for further state estimation. In the feedback off case the steer-

ing feedback information is lost.

Despite the change in the dynamics of the upper handlebar the response of the rider is almost identical. Thereupon, we assume that the internal controller of the rider is either adaptive or is driven by some combination of torque or position control. In the case of torque control this would mean complete re-adaptation of feedback gains which would have resulted in some kind of adaptation period for the participants when they swapped steering configurations. Although, no adaptation period was needed for any of the participants. Alternatively, in the case of position control steer angle increments are feed-through an inverse model of the steering assembly to produce the necessary forcing element. In this case, switching between configurations, would mean re-adaptation of the internal model of the handlebar assembly. This is much more plausible as it mainly concerns tuning of the internal perception of handlebar inertia which can happen instantaneously. To reveal if the later assumption is true an additional study that models the rider as position and torque controller will be conducted. The identified parameters of the former and later controller might lead into further insights regarding the conclusions of this study.

All data and supplemental material related to this article is available online at <https://doi.org/10.5281/zenodo.3365351> (Dialynas et al., 2019).

3

RIDER CONTROL IDENTIFICATION IN BICYCLING USING GRAY BOX APPROACH

3.1. INTRODUCTION

Balancing a bicycle in motion is an acquired skill which is poorly understood. From the first appearance of the modern bicycle in the late 1880s until now, dynamic models of uncontrolled bicycles have provided fundamental insight into bicycle stability in relation to speed and geometry[18, 25]. Further research into human control is needed to design safer bicycles and explore the potential of new safety systems. In depth-analysis of the rider sensory dynamics including delays and thresholds are necessary to probe the dynamics of the rider-bicycle balance control mechanism.

Research in the field of cybernetics started in the 1950s to advance aircraft technology and understand pilot control. McRuer and Krendel [22] were one of the first who tried to model the human operator as a servo system element with time delay. The so called "McRuer cross over model" was later extended to the "McRuer precision model" which accounted for low frequency neuromuscular lags [23]. Results showed that the human tries to adapt its control strategy in order to achieve a first order integrator open loop transfer function near the systems cross-over frequency. Among the first researchers who focused in the manual control of bicycles were Van Lunteren et al. [38]. They used a stationary bicycle simulator and system identification techniques to identify the rider control at a constant speed of 4.2 m/s . They described the rider as a proportional– integral–derivative (PID) position controller with delay. Although, their results are questionable since the bicycle simulator had no visual display and the obtained controller has not been experimentally validated. Roland [29], Roland Jr and Daniel [30] developed a bicycle stability and path following torque controller. The controller consisted of an inner and outer loop responsible for roll stabilization and lateral tracking, respectively. The stabilization controller was described as a PID with delay, whereas the tracking controller as a simple proportional controller. Results showed adequate performance but validation of the simulated responses has not been examined yet. Weir [40] developed a cross-over model for Sharp's [34] motorcycle model in order to identify the transfer functions of the various control input–output relations. He concluded that steer torque response to lean angle error is the easiest way to balance a motorcycle in motion. Eaton [7] later conducted experiments to validate both the theoretical motorcycle model of Sharp [34] and rider model of Weir [40] . Despite the fact that, he excluded the lean torque and used only the inner roll stabilization loop as a control input, results showed that low uncertainty was present in the estimated control parameters and low discrepancy in the fitting of the steer torque responses. Hess et al. [15] attempted to introduce a task independent handling qualities metric for bicycle control. For this reason, he developed a model with five gains, two fixed second-order filters, and a preview time. Schwab et al. [33] recently tried to model the bicycle rider using lateral force perturbation experiments. A rider control model applying steering torque at the handlebars has been developed to explore the potential feedback of sensory cues during the bicycle balancing task. The identified rider control parameters, after model reduction, stabilize the system and mimic realistic rider control behavior.

The majority of aforementioned modeling approaches represent the rider as a torque controller and incor-

porate system delays. Albeit, the selected delays do not attribute directly to the physical response time of the visual, vestibular and proprioceptive system. Furthermore, none of these models include any type of internal model control (IMC) as frequently happens in most of human motor control studies [9, 10, 12, 41]. Consequently, the ability of humans to adapt and altered steering dynamics even when feedback is intermittent or delayed has never been examined. Aside from that, the effect of haptic steering feedback in the balancing of bicycling has never been examined parametrically . Therefore, the role of the sensory receptors and in particular of the proprioception muscle splindles (position feedback) and golgi tendon organs (force feedback) during the riding process remains a black box .

The aim of this study is to evaluate the performance of three different control approaches with increased complexity and also examine the effect of handlebar torque feedback during the steering and balancing task. The performance of all models are compared with the experimentally derived non-parametric finite impulse responses (FIR's) of Dialynas et al. [5]. Two metrics are used to assess the performance of the three controllers and to analyse the impact of torque feedback on rider control. The covariance coefficient (CV) of the estimated controller parameters is used as a measure of uncertainty, whereas the variance accounted (VAF) as a measure of fitting between the simulated and actual responses .The paper is organized as follows: First, the experimental set-up and experimental procedure are presented. Next, the methods and results, are presented. The article ends with a discussion and conclusion section highlighting the main findings of this research.

3.2. METHODS

In this work system identification techniques are employed to investigate the effectiveness of torque feedback via a gray box analysis of a rider control model. The ultimate goal is to formulate a model that best simulates bicycle rider balance behavior. This is done by comparing the parametric results of three torque feedback level conditions. In the first, the torque feedback loop is part of the rider control model. In the second, it is removed by setting its corresponding gain value to zero. In the third, the effectiveness of torque feedback is reduced by altering the plant dynamics and creating a steering configuration where the forces that would naturally transfer from the front wheel contact point to the handlebars are canceled, similar to how the haptics off case was implemented in the experimental condition [5]. The full methodology is summarized in the list below:

1. Black box identification : the procedure described in [5] is followed to produce impulse response functions (IRFs), through the use of a FIR model, for steering angle δ , roll angle ϕ , yaw angle ψ and steer torque T_δ . This is done in order to extract the linear relationship between disturbance and measurements effectively filtering intrasubject variability. In the case of T_δ instead of considering the whole bicycle rider closed loop system as a black box, the bicycle rider open loop is chosen with input the disturbance w and output the control input T_δ (see figure 3.1).
2. The produced IRFs $h^\delta(\tau)$, $h^\phi(\tau)$, $h^\psi(\tau)$, $h^{T_\delta}(\tau)$ are filtered using zero-phase low pass filter with a cutoff frequency of 10 Hz.
3. The complete dataset is split into a training and a validation subdataset. The IRFs are averaged over each subdataset's participants in order to produce 2 mean rider responses. The variance accounted for VAF, between each individual's response and the mean rider's, is calculated. The rider with the highest VAF for all outputs across all speed levels is chosen as the median rider of each dataset. All further parameter estimation is conducted on the response of the median rider of the training dataset. Analysis is chosen to be conducted on the median rider since intersubject variability was low as is shown in [5].
4. The IRFs of the median rider are convolved with the measured disturbances of each run to produce the non-parametric output $y_\delta(t)$, $y_\phi(t)$, $y_\psi(t)$, $y_{T_\delta}(t)$.
5. Zero Delay Model gray box identification: A gray box model is fit to the measured lateral force and the filtered response of the FIR model for each run. This is repeated for three conditions. In the first, the control process dynamics approximate a normal bicycle and will be referred to as haptic feedback on (haptics on), while the rider has the torque feedback loop connected. In the second, the control process dynamics approximate again a normal bicycle, but the internal torque feedback loop of the rider is severed. In the third condition the steering dynamics change to that of steer-by-wire. This means that the coupling between roll and steer dynamics is modified. The rider is only receiving feedback due to

the inertia of the handlebar and motor drive components. This condition is referred to haptic feedback off (haptics off).

6. Variable Delay Model gray box identification: The model is updated with time delays. The model is fit to the measured lateral force and the filtered response of the FIR model for each run. This is repeated for the three conditions described above.
7. Variable Delay Reafferent Optimal Prediction (VDROP) Model gray box identification: The gray box model is updated with a delay compensation algorithm. The model is fit to the measured lateral force and the filtered response of the FIR model for each run. This is repeated for the three conditions described above.
8. Assessment on the importance of torque feedback is made based on the the normalized covariance of the identified gray box parameters and the change of *VAF* in the lateral force to steer angle fit between conditions.
9. Assessment on the delay compensation strategy used is made based on the fitting performance across gray box models. Additionally the predictor is compared with a more conventional approach found in motor control literature. Finally the predictive capability of the VDROP model is tested by comparing its results with the median rider of the validation dataset.

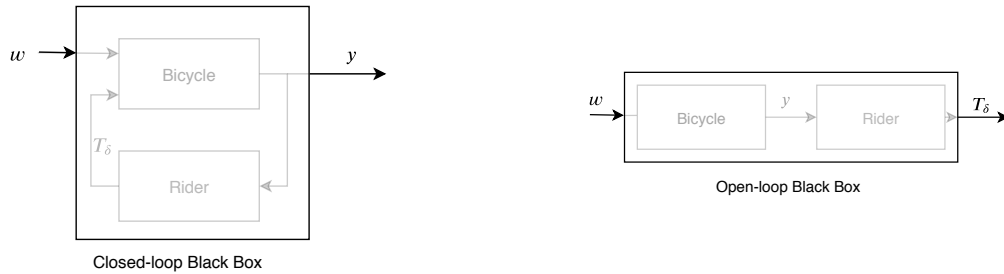


Figure 3.1: The bicycle rider closed loop black box system used in the FIR model for extracting the linear relationship between disturbance w and outputs ϕ, δ, ψ (left). The bicycle rider open loop black box system used in the FIR model for extracting the linear relationship between disturbance w and control input T_δ (right).

3.2.1. BICYCLE MODEL

The bicycle model used is the so called Whipple-Carvalho model the dynamics of which have been expressed in a set of linearized equations by Meijaard et al. [25]. In the original model three assumptions are made. The first is that the rider is rigidly attached in the saddle with the mass of the arms and legs acting as a point. Secondly, the contact between tire and ground is modeled as a non slipping rolling point contact meaning that the wheels can rotate without lateral slip. Lastly it is assumed that the total energy of the system is preserved. The resulting non-holonomic mechanical model has three velocity degrees of freedom, the forward speed, the rear frame roll rate $\dot{\phi}$ and the steering rate $\dot{\delta}$. The lateral motion is described by two coupled second order differential equations given by equation (3.1).

$$\mathbf{M}\ddot{\mathbf{q}} + \nu\mathbf{C}_1\dot{\mathbf{q}} + [\mathbf{g}\mathbf{K}_0 + \nu^2\mathbf{K}_2]\mathbf{q} = \mathbf{f} \quad (3.1)$$

where \mathbf{q} is a vector containing the roll and steer angles, \mathbf{f} is a vector containing the roll and steer torques, g is the gravitational acceleration and \mathbf{M} , $\nu\mathbf{C}_1$, $\mathbf{g}\mathbf{K}_0 + \nu^2\mathbf{K}_2$ are the "mass", "damping" and "stiffness" ratios in matrix form respectively. The entries in the constant coefficient matrices $\mathbf{M}, \mathbf{C}_1, \mathbf{K}_0, \mathbf{K}_2$ are calculated from a set of 25 bicycle parameters related to inertial and design properties of the steer by wire bicycle (see table 3.5).

To determine the stability of the open loop system in a straight ahead motion the characteristic polynomial derived from

$$\det(\mathbf{M}\lambda^2 + \nu\mathbf{C}_1\lambda + \mathbf{g}\mathbf{K}_0 + \nu^2\mathbf{K}_2) = 0 \quad (3.2)$$

is solved for a forward speed range from 0 to 10 ms^{-1} where λ are the eigenvalues of the system (see figure 3.3). The two interesting eigenmodes defined by the locus plot are the weave and capsise. The weave

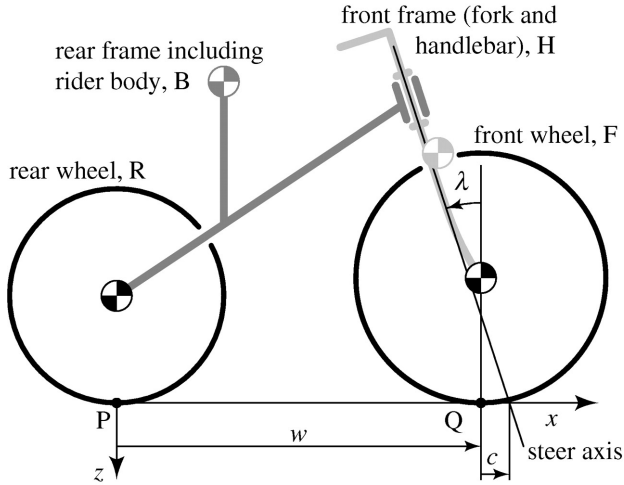


Figure 3.2: The Whipple-Carvalho bicycle model consists of four rigid bodies: rear wheel R, rear frame B, front frame H and front wheel F connected via hinges. The center of mass locations are expressed relative to the x - and z -coordinates shown (with origin at P and y pointing towards the reader). The other parameters shown are the steer axis tilt λ , wheelbase w and trail c . The model at its most expanded form is described by 25 parameters.[25]

corresponds to an oscillatory mode as can be seen by the existence of imaginary parts and represents a motion in which the bicycle sways about its heading. The oscillatory motions exponentially fades when forward speed is larger than 4.39 ms^{-1} . The capsize on the other hand has an eigenvector dominated by lean and leads to a gradual roll drift to infinity when the eigenvalue crosses the zero line around 6.67 ms^{-1} . Since in

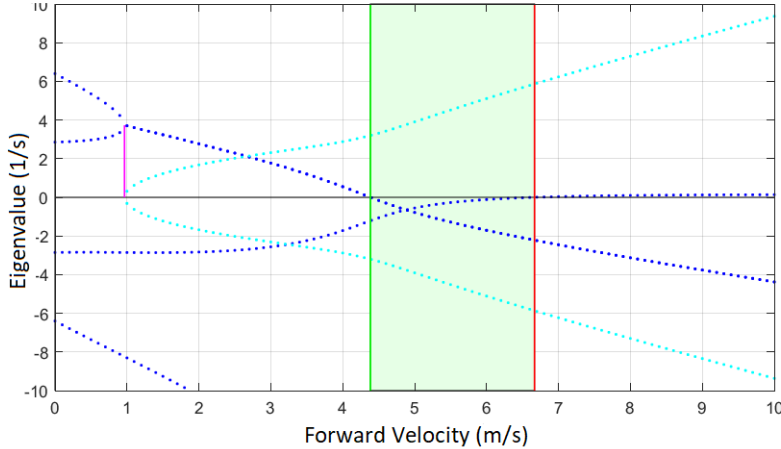


Figure 3.3: Root locus plot of the steer by wire bicycle. Dotted blue lines indicate the real part of the eigenvalues while dotted cyan show the imaginary part. The stable region corresponds to speeds $4.39 \lesssim v \lesssim 6.67 \text{ ms}^{-1}$

the experimental setup the task could not be isolated to purely balance the equations are extended to include heading. Heading is defined as a linear combination of steer angle and steer rate as expressed by Meijaard et al. [25] in equation (3.3).

$$\dot{\psi} = \frac{v\delta + c\dot{\delta}}{w} \cos \lambda \quad (3.3)$$

When modeling the haptics off case of the steer-by-wire bicycle the dynamics of the plant need to change accordingly. In that configuration, the forcing steering input is directly proportional to steering acceleration,

for this reason the second of the set of equations in 3.1 becomes :

$$M_{22}\ddot{\delta} + M_{21}\ddot{\phi} + \nu C_{122}\dot{\delta} + \nu C_{121}\dot{\phi} + [gK_{022} + \nu^2 K_{022}]\delta + [gK_{021} + \nu^2 K_{021}]\delta = T_\delta \quad (3.4)$$

$$M_{22}\ddot{\delta} = T_\delta \quad (3.5)$$

$$I_{F_{xx}}\ddot{\delta} = T_\delta \quad (3.6)$$

where $I_{F_{xx}}$ is the moment of inertia of the decoupled handlebar assembly.

For control purposes equation (3.1) is expressed in state space form with state vector $\mathbf{x} = [\dot{\phi}, \dot{\delta}, \phi, \delta, \psi]^T$, forcing input $\mathbf{f} = T_\delta$ and output equal to the full state. The bike is assumed to be controlled only by a steering torque because according to both Moore [28] and Weir [40] the rear frame roll angle is mainly controlled by steering.

$$\dot{\mathbf{x}} = \mathbf{Ax} + \mathbf{B}T_\delta + \mathbf{H}_d w \quad (3.7)$$

$$\mathbf{y} = \mathbf{Cx} + \mathbf{DT}_\delta \quad (3.8)$$

where matrices A, B, C, D, H_d are defined by:

$$\mathbf{A} = \begin{bmatrix} -\mathbf{M}^{-1}\nu\mathbf{C}_1 & -\mathbf{M}^{-1}(g\mathbf{K}_0 + \nu^2\mathbf{K}_2) \\ \mathbf{I}_2 & \mathbf{0} \\ 0 & 0 \end{bmatrix}, \mathbf{B} = \begin{bmatrix} \mathbf{M}^{-1} \\ \mathbf{0} \end{bmatrix} \quad (3.9)$$

$$\mathbf{C} = \mathbf{I}_5, \mathbf{D} = \mathbf{0} \quad (3.10)$$

$$\mathbf{H}_d = \begin{bmatrix} \mathbf{M}^{-1} \begin{bmatrix} l_g \\ c_s \end{bmatrix} \\ \mathbf{0} \end{bmatrix} \quad (3.11)$$

\mathbf{H}_d is the matrix defining the dynamics of the lateral disturbance w . In this case the force application point was l_g distance from the ground. The constant c_s coefficient is due to the coupled roll to steer dynamics and is selected as a fraction of w similar to Schwab et al. [33]. This results in an additional torque perturbation T_δ in the handlebars.

3.2.2. RIDER CONTROL MODEL

The complete high level overview of the model is shown in figure 3.4. The output state of the bicycle is concatenated with the steering torque to produce the complete vector of sensory inflow. The measurements attributed to the vestibular, visual and proprioceptive system of the human body are delayed and fed into a prediction algorithm that uses an internal model of the process dynamics to forward the measurements in time. This is made possible by the use of the efference copy, which is an internal copy of an outflowing, movement-producing signal generated by the motor system. The controller is just a pure gain block with free parameters to be estimated through gray box system identification. The final control forcing input is produced after passing through a transfer function simulating the neuromuscular dynamics.

The neuromuscular dynamics block works as a second order filter to simulate the limitations of the human response. In state space form this block is expressed by :

$$\dot{x}_{nm} = \begin{bmatrix} 0 & 1 \\ -\omega_c^2 & -2\zeta\omega_c \end{bmatrix} \begin{bmatrix} T_\delta \\ \dot{T}_\delta \end{bmatrix} + \begin{bmatrix} 0 \\ \omega_c^2 \end{bmatrix} a \quad (3.12)$$

$$y_{nm} = [1 \ 0] \begin{bmatrix} T_\delta \\ \dot{T}_\delta \end{bmatrix} \quad (3.13)$$

where a is the controller output representing the efferent neural signal, ζ is the damping coefficient and ω_c is the cutoff frequency. The latter two parameters are chosen according to activation dynamics present in the shoulder joint [13].

The steer angle δ and steer rate $\dot{\delta}$ feedback is attributed to the muscle spindles, while the torque feedback is made possible with the help of the golgi tendon organs. The roll and heading angle come from the visual system. Lastly the roll rate feedback is attributed to the vestibular system.

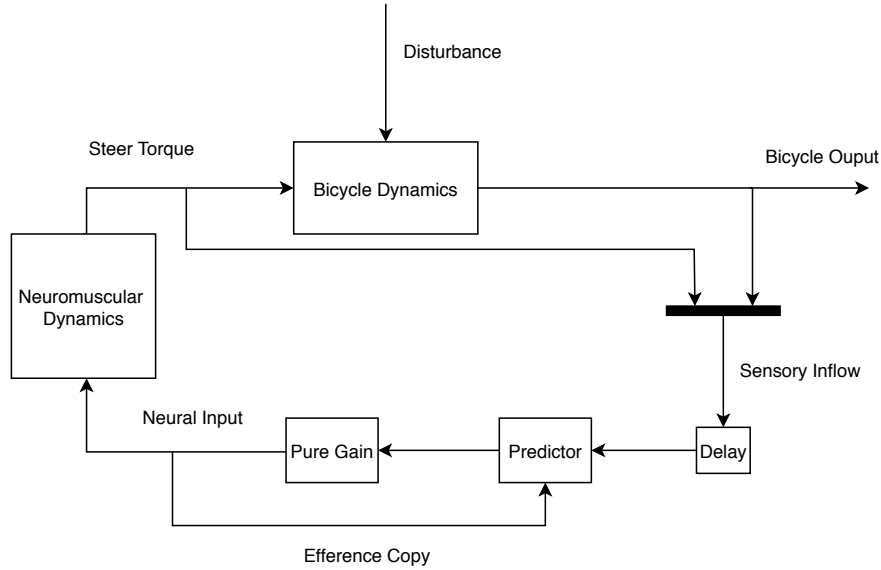


Figure 3.4: Block diagram of the complete rider-bicycle model.

The bicycle model of equation (3.7) is combined with the neuromuscular dynamics block of equations (3.12) and (3.13) to create a combined plant with state $x = [\dot{\phi}, \dot{\delta}, \phi, \delta, \psi, T_\delta \dot{T}_\delta]^T$, input a and w and output $y = [\dot{\phi}, \dot{\delta}, \phi, \delta, \psi, T_\delta]^T$. In order to make possible the implementation of the predictor which is discrete in nature the state space representation of the combined plant is discretized by zero order hold with a time step of 0.001 s. The equivalent model block diagram is shown in figure 3.8.

THE REAFFERENT OPTIMAL PREDICTOR

Many strategies to counter time delays have been proposed in literature. The most basic predictor is the Smith predictor, which has been explored in motor control research by Miall et al. [26]. The Smith predictor compensates for time delays through the use of an internal forward model of the controlled dynamics and an internal model of the sensory delay pathways. The forward model works by utilizing an efferent signal of the control input while the comparison between prediction and measurement is trying to simulate the human's ability to distinguish between reafference and exafference. Unfortunately the most basic Smith predictor scheme does not work for unstable open loop systems [35]. In this work a modification to the normal Smith predictor scheme is suggested. In place of the forward model a discrete optimal predictor (DOP) is used that forward simulates the amount of steps according to the model of sensory delay (see figure 3.6). This works like a resetting forward model that is updated every time step by the delayed state so the predictor loop does not become unstable. Because every sensory pathway has different time delays, the conventional DOP is adapted to work with variable time delay state input. This adaptation is illustrated with a simplified example in the block scheme of figure 3.7. The DOP predictor without the Smith correction can still work and has been implemented by van der Kooij et al. [37] for modeling stance control but it leads to predictions that do not contain any amount of the effect of the disturbance on the state. The block diagram of the predictor can be seen in figure 3.8.

3.2.3. PARAMETER ESTIMATION

In order to assess the effectiveness of the torque feedback loop, three models of incremental complexity are used. In the first the feedback pathways are fed into the controller without delays. In the second delays are added. The third one compensates for time delays by the use of the VDROP. The three models have the controller gains as free parameters. More specifically, the gains are estimated by fitting the model output into the

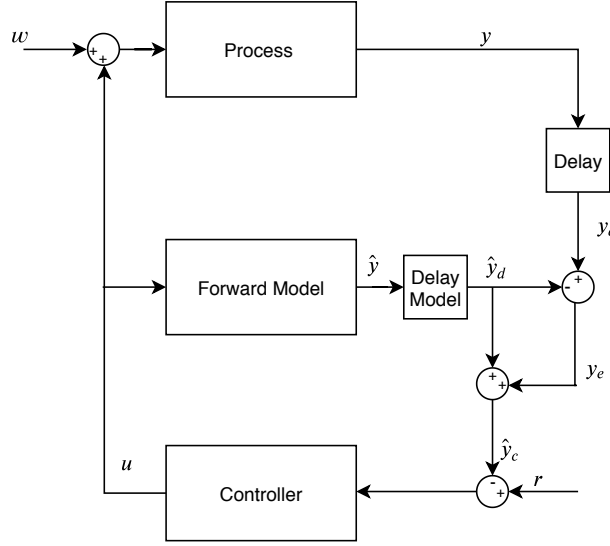


Figure 3.5: Block diagram of the basic Smith Predictor scheme. The Smith Predictor uses an internal forward model to predict the delay-free response \hat{y} of the process. It then compares this prediction with the desired setpoint r to decide what adjustments are needed (control u). To prevent drifting and reject external disturbances, the Smith predictor also compares the actual process output with a prediction \hat{y}_d that takes the dead time into account. The gap $y_e = y_d - \hat{y}_d$ is fed back and contributes to the overall controller input. Note that y_e amounts to the perceived state mismatch delayed by the duration of dead time.

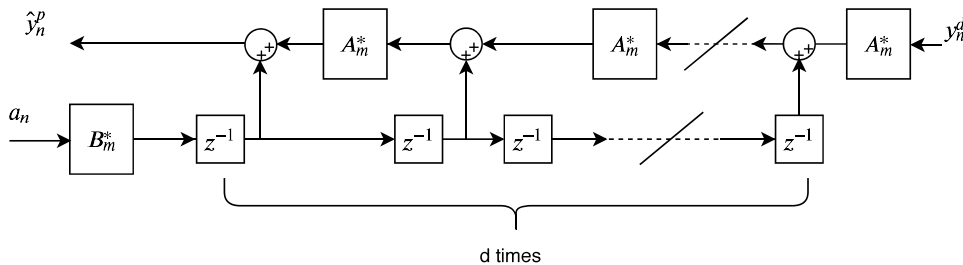


Figure 3.6: The discrete optimal predictor consists of a tapped delay line. The tapped delay line used in this work is a forward simulation of the discretised dynamics of the bicycle including neuromuscular dynamics. It uses the efference copy of the known previous control input a_n and the delayed estimate y_n^d . A_m^* and B_m^* are the best available discrete approximation of these dynamics.

non-parametric data-set derived in [5]. The gains were estimated by minimization of the cost function

$$V_N(\boldsymbol{\theta}) = \frac{1}{N} \sum_{k=1}^N \left[64 \frac{(\hat{y}_k^\delta(\boldsymbol{\theta}) - y_k^\delta)^2}{\max_k(y_k^\delta)^2} + 11 \frac{(\hat{y}_k^\psi(\boldsymbol{\theta}) - y_k^\psi)^2}{\max_k(y_k^\psi)^2} + 7 \cdot 10^{-6} \frac{(\hat{y}_k^{T_\delta}(\boldsymbol{\theta}))^2}{\max_k(y_k^{T_\delta})^2} \right] \quad (3.14)$$

where $\boldsymbol{\theta}$ is a vector containing all the free parameters, \hat{y}^δ and \hat{y}^ψ are the outputs of the simulation for the measured external disturbance w and the vector of parameters $\boldsymbol{\theta}$ for steer angle δ and heading angle ψ respectively, while y^δ and y^ψ are the outputs of the non-parametric model.

The first two terms of the cost function are trying to match the steering and heading response of the para-

metric model with that one of the non-parametric model, while the third one minimizes the amount of input torque generated in order to produce the best possible fit while maintaining minimal control effort. The weights are chosen heuristically. For optimization the genetic algorithm with a fitness limit of 0.03 is first used in order to produce a good starting parameter vector for gradient descend algorithm to take over, which finally finds the closest possible estimate of the global minimum. For the genetic algorithm a crossover fraction of 0.85 along with a population size 10 times the length of the parameter vector is used.

The gains attributed to the muscle spindle sensors (K_δ and $K_{\dot{\delta}}$) are constrained to be only positive. The assumption is that they work like a delayed steering stiffness and damping. Additionally, the gains K_ψ and K_ϕ are constrained to fall under -250 and 250 $\text{kg m}^2 \text{s}^{-1}$. When left unconstrained these parameters drive the whole gain vector to unrealistic values for insignificant amount of fitting performance increase (< 0.1%).

The impulse response function of the median rider is used. This is determined by taking the mean impulse response function of each measured output and finding the participant which had the highest variance accounted for between the individual response and the mean across all speed levels for all filtered outputs. Each system was identified for three different model conditions:

1. 6 feedback pathways including torque feedback
2. 5 feedback pathways excluding torque feedback
3. 6 feedback pathways including torque feedback but bicycle dynamics are switch to "haptics off".

In the third condition the internal model used in the predictor is not updated to reflect the changed bicycle dynamics. This assumption is made due to the fact that no adaptation time was noted in the experiments for any of the participants when switching the steering configurations so significant tuning of an internal model is not realistic.

As metric of model validity the variance accounted for between parametric and non-parametric output is used, defined as

$$\text{VAF}_d(\boldsymbol{\theta}) = 1 - \sum_{k=1}^n \left(y^d(k) - \hat{y}^d(k, \boldsymbol{\theta}) \right)^2 / \sum_{k=1}^n \left(y^d(k)^2 \right) \quad (3.15)$$

where $d = \{\phi, \delta, \psi\}$.

In order to assess the importance of the torque feedback, the uncertainty of each parameter is found. Parameters with the lowest uncertainty contribute more to the fit so they are deemed more important. To find the uncertainty the covariance matrix is estimated from :

$$\text{cov}_{\hat{\theta}} = V_N(\hat{\boldsymbol{\theta}}) \mathbf{H}(\hat{\boldsymbol{\theta}})^{-1} \quad (3.16)$$

$$\text{with } \mathbf{H}(\hat{\boldsymbol{\theta}}) = \frac{\partial^2 V_N}{\partial \theta_i \partial \theta_j} \quad (3.17)$$

where $\hat{\boldsymbol{\theta}}$ is the closest estimate to the true parameter vector $\boldsymbol{\theta}^*$ that produces the true global minimum and \mathbf{H} is the hessian matrix numerically estimated by the gradient descend algorithm. However, since bigger parameters are going to have naturally larger variances the diagonal values are normalized by the parameter value to produce the coefficient of variation.

$$CV_i = \sqrt{\frac{\sigma_{\hat{\theta}_i}^2}{\hat{\theta}_i^2}} \quad (3.18)$$

where $\sigma_{\hat{\theta}_i}^2$ are the diagonal elements of $\text{cov}_{\hat{\theta}}$.

3.3. RESULTS

3.3.1. ZERO DELAY MODEL

The results of the zero delay model for the median rider are presented in table 3.2. A VAF of over 90 % is easily achieved for both steer angle and heading, while for roll the discrepancy is larger. A look into how the

model approximates the measured rider input and bicycle states for all forward speeds is seen in figures 3.9 and 3.10. Even in the ideal case with zero delays, the model inputs seems to lag behind the measured applied rider torque.

From the coefficient of variation, no real difference between the levels of normalized uncertainty is noted. However, VAF_δ drops more than 15-20% when T_δ feedback is turned off (see table 3.2), which indicates significant impact on the fit. Additionally, the steering angle and torque response becomes significantly more oscillatory when T_δ feedback is turned off (see figure 3.11). Roll stabilization performance does not seem to be affected, however steering effort considerably does. Regarding the haptics off case, where the intent is to simulate the steering feel the participants experienced in the second experimental condition, the level of steering fit degradation is small (< 3%).

3.3.2. VARIABLE DELAY MODEL

The same procedure is repeated for the gray box model but now introducing delays in all feedback pathways. For δ and $\dot{\delta}$ which are attributed to the muscle spindle sensors and for the torque feedback which is attributed to the golgi tendon organs a delay of 25 ms is chosen [4, 36]. For the feedback states attributed to visual feedback such as the roll angle ϕ and yaw angle ψ a much greater delay of 200 ms is chosen [16]. Finally for the vestibular roll rate feedback a delay of 50 ms is implemented [1].

The results of the variable delay model for the median rider are presented in table 3.3. Despite the fact that significant delay is introduced into the system the torque feedback loop manages to compensate maintaining a VAF_δ of over 90 % for low speed levels (see table 3.3 and figure 3.12). In figures 3.12 and 3.13 the delayed response of the simulated compared to the real rider is visible between the red and blue lines in the rider torque graph. This is further exaggerated in the two remaining conditions resulting in much more oscillatory steering responses with a visible impact on roll stabilization (see figure 3.14). The coefficient of variation of the K_δ parameter in the haptics on with T_δ feedback connected is the highest especially for the two highest speed levels, which indicates that this parameter is not significant for the fit. Between T_δ feedback on and feedback off, a much larger drop in VAF is noted. Additionally, contrary to the zero delay model an equally significant drop in the fit is noted for the haptics off case.

3.3.3. REAFFERENT OPTIMAL PREDICTION MODEL

The VDROP model of figure 3.8 is implemented with a consistent time delay among sensory pathways equal to 50 ms. Adaptation of the predictor to work with variable time delays is not part of the scope of this work. It is assumed that the internal model of bicycle and neuromuscular dynamics along with the internal model of the inherent time delay responsible for prediction is perfect for controlling the normal bicycle dynamics ($A^* = A_m^*$). However in the haptics off case, where the steering dynamics change, the internal model is not updated in simulation on purpose. This falls inline with what was noted during the experiments where the subjects adapted to the new bicycle dynamics instantaneously, so a full "re-calibration" of the forward model is too far fetched. This way the extent to which the smith prediction principle can counter forward model inaccuracies is also tested.

The optimization results for the VDROP model are presented in table 3.4 for the median rider. From the VAFs and the signals shown in figures 3.15 and 3.16 it is visible that the quality of the fit is comparable with the ideal zero delay case. In the haptics on with T_δ feedback condition K_δ shows disproportionately higher CV which indicates lower importance for the fit for the steering rate feedback. However, in the haptics on without K_{T_δ} feedback case, the gain K_δ shows the highest uncertainty (see table 3.4). Similar drop in VAF_δ is present as in the zero delay model when T_δ feedback is turned off, which shows significant importance of the golgi tendon organ sensory pathway. Furthermore, the steering response exhibits the same oscillatory behavior when torque feedback is completely disabled (see figure 3.17). However, the predictor manages to compensate in the haptics off case and achieve good fit which is not present in the variable delay model (see table 3.4). In figure 3.21 the gains estimated for the median rider as a function of speed for all torque feedback conditions are presented. Consistent trends could only be discerned for the heading gain K_ψ .

In figures 3.18 to 3.19 a complete comparison between rider models for all feedback conditions is presented. The response shown is the result of the first lateral perturbation of each individual run. The zero delay and prediction models exhibit almost identical responses as it was evident from the over 90% fit achieved. The variable delay model lags behind in both the produced control input and bicycle output, as is expected. Worth noting the lag in the control input of the prediction model in the first few milliseconds after the perturbation.

Despite that fact the VDROP model compensates and achieves similar output as the idealized zero delay case. This is a result of the fact that no matter how good the prediction algorithm is the human has no knowledge of the future so the response from the controller will start after the first state information arrives from the feedback pathways which are delayed. The forward model in this case does not help predict the state as it has no information of the external disturbance.

Finally, in order to assess the effectiveness of the Reafferent Optimal Predictor, the VDROP model is compared with an implementation of the prediction algorithm without the smith correction, meaning the predictor consists of just the adapted DOP (see figure 3.7). For the comparison the gains estimated from the zero delay model are used, so as to remove any potential adaptation that might give the VDROP model an advantage. The effect of the undelayed estimate using both approaches is seen in figure 3.20a

From the left plot of figure 3.20a it is visible that the estimate of the state improves due to the fact that the effect of the disturbance on the state albeit delayed is added back to the optimal prediction. Worth noting that both prediction strategies produce satisfactory results and manage to stabilize the system. However, the main advantage of VDROP is its ability to correct for internal model inaccuracies. In figure 3.20 the results of a simulation using VDROP model is compared with the results of the discrete optimal predictor but in this case internal model imperfections are introduced. This is done by replacing the perfect forward model with the one used for the haptics off steering dynamics. The reasoning behind that is based on the assumption that the human has a reduced perception of bicycle dynamics that does not take into account the fact that roll also affects the state of the handlebar assembly. In figure 3.20b it is visible that VDROP manages to achieve comparable performance to the perfect internal model case while DOP fails.

VALIDATION

Similar to how the median rider of the training dataset is calculated, the median rider of the validation dataset is determined. The VDROP model with its estimated parameters is tested by determining the variance accounted for between the non-parametric response of the validation dataset and the simulation output. The results can be seen in table 3.1.

Table 3.1: VAFs between the simulation output and the non-parametric response of the median rider of the validation dataset for all forward speed levels.

v (m s ⁻¹)	VAF_ϕ	VAF_δ	VAF_ψ
2.5	70.53	89.41	91.91
3.7	72.42	83.44	96.78
4.4	71.78	95.96	88.68
5.6	72.06	88.99	90.02

3.4. DISCUSSION

Since in the control scheme the feedback is defined as negative, positive feedback gains produce torques opposite to the direction of the state that they act on. In that case a positive K_δ works like a normal restoring spring and a positive K_ψ as a dissipative damper. This was a design choice for all gains related to muscle spindles, in order to simulate lower spinal reflexes which lead to increased stiffness and damping of the handlebar assembly. This is the reason the index of dispersion for the gain K_δ is so large for the cases where the estimate is near zero (see table 3.3). The gradient descent algorithm if left unbounded would result in values lower than zero which would lead to a physiologically impossible reflex response.

On the other hand, the proportional and derivative roll gains are consistently negative among all models for all forward speeds and all torque feedback level conditions. This falls in line with what is believed to be the main balancing strategy for single track vehicles; the so called "steer into the fall". K_ψ always being negative means that the rider steers into the direction that heading is diverging, which seems counter intuitive. However, this could be explained by the fact that the heading correction task and the roll stabilization are inherently coupled. K_ψ also exhibits a consistent trend in all feedback conditions in all the rider models test. It decreases as the forward speed increases (see figure 3.21). This might indicate that heading is what modulates the response as forward speed increases. As forward speed increases and the bicycle becomes more and more stable the rider shifts focus towards heading correction and less towards roll stabilization.

Table 3.2: Results for the zero delay model as estimated for the median rider for all speed levels. Results are presented for the three conditions. Haptic on/off differentiates based on the dynamics of the bicycle model, while "with or w/o T_δ feedback" differentiates based on the structure of the rider control model. The values of the gains are presented as well as their corresponding uncertainty level measured by the coefficient of variation CV_i . Additionally, the variance accounted for of the orientation outputs between parametric and non parametric signals is also presented. The derivative gains ($K_{\dot{\phi}}, K_{\dot{\delta}}$) are measured in $\text{kgm}^2 \text{s}^{-2}$ while the proportional gains (K_ϕ, K_δ, K_ψ) are measured in $\text{kgm}^2 \text{s}^{-1}$. The torque feedback gain K_{T_δ} is dimensionless.

		Bicycle →		Haptic On		Haptic Off		
		Rider →	with T_δ feedback	w/o T_δ feedback		with T_δ feedback		
Forward Speed			Value	$CV(10^{-4})$	Value	$CV(10^{-4})$	Value	$CV(10^{-4})$
2.8 ms^{-1}	$K_{\dot{\phi}}$	-77.17	114.86	-22.46	29.77	-115.36	213.52	
	$K_{\dot{\delta}}$	2.26	73.57	2.58	18.93	8.76	187.30	
	K_ϕ	-164.88	132.25	-24.50	73.14	-248.24	217.05	
	K_δ	32.75	150.14	3.76	140.96	29.67	215.07	
	K_ψ	-63.22	133.29	-9.85	53.71	-93.44	223.02	
	K_{T_δ}	3.51	176.20	-	-	7.53	223.83	
	VAF_ϕ	77.80		82.79		78.37		
	VAF_δ	98.34		79.19		98.20		
	VAF_ψ	93.46		93.51		93.74		
3.6 ms^{-1}	$K_{\dot{\phi}}$	-109.94	146.98	-21.30	35.99	-78.28	61.00	
	$K_{\dot{\delta}}$	8.22	139.00	3.30	24.78	9.09	51.11	
	K_ϕ	-248.47	147.39	-34.64	71.54	-229.14	84.40	
	K_δ	50.78	147.72	6.48	130.57	53.16	92.96	
	K_ψ	-132.13	152.08	-17.74	61.92	-103.75	74.49	
	K_{T_δ}	4.52	167.24	-	-	6.89	64.17	
	VAF_ϕ	79.92		85.93		80.89		
	VAF_δ	98.83		86.40		97.08		
	VAF_ψ	95.33		97.95		95.15		
4.7 ms^{-1}	$K_{\dot{\phi}}$	-92.50	117.34	-27.29	46.40	-102.63	40.87	
	$K_{\dot{\delta}}$	4.81	183.05	4.25	41.56	11.24	28.38	
	K_ϕ	-183.03	135.64	-38.17	76.43	-249.74	74.10	
	K_δ	22.57	237.51	2.65	591.87	63.36	88.33	
	K_ψ	-165.42	126.89	-33.78	63.74	-188.67	58.81	
	K_{T_δ}	3.42	174.23	-	-	8.98	13.88	
	VAF_ϕ	77.03		83.06		78.60		
	VAF_δ	97.57		80.27		95.57		
	VAF_ψ	91.41		97.03		92.48		
5.7 ms^{-1}	$K_{\dot{\phi}}$	-83.90	117.61	-31.12	43.99	-76.30	47.12	
	$K_{\dot{\delta}}$	5.83	142.87	5.58	40.62	10.91	30.23	
	K_ϕ	-166.08	127.89	-43.64	67.14	-208.33	83.09	
	K_δ	14.85	98.10	1.14	1836.39	79.44	75.47	
	K_ψ	-186.77	128.56	-49.82	52.31	-176.96	69.82	
	K_{T_δ}	3.24	185.07	-	-	8.45	29.67	
	VAF_ϕ	79.17		84.03		80.30		
	VAF_δ	97.51		84.09		94.71		
	VAF_ψ	90.97		96.41		91.56		

Table 3.3: Results for the variable delay model as estimated for the median rider for all speed levels. Results are presented for the three conditions. Haptic on/off differentiates based on the dynamics of the bicycle model, while "with or w/o T_δ feedback" differentiates based on the structure of the rider control model. The values of the gains are presented as well as their corresponding uncertainty level measured by the coefficient of variation CV_i . Additionally, the variance accounted for of the orientation outputs between parametric and non parametric signals is also presented. The derivative gains (K_ϕ, K_δ) are measured in $\text{kgm}^2 \text{s}^{-2}$ while the proportional gains (K_ψ, K_{T_δ}) are measured in $\text{kgm}^2 \text{s}^{-1}$. The torque feedback gain K_{T_δ} is dimensionless.

Bicycle →		Haptic On			Haptic Off	
Rider →	with T_δ feedback	w/o T_δ feedback		with T_δ feedback		
Forward Speed	Value	CV (10^{-4})	Value	CV (10^{-4})	Value	CV (10^{-4})
2.8 ms^{-1}	K_ϕ	-68.53	38.72	-14.93	37.52	-28.19
	K_δ	2.09	110.32	2.30	32.17	2.65
	K_ϕ	-146.29	72.07	-16.98	92.51	-79.20
	K_δ	22.18	95.38	4.62	103.75	10.51
	K_ψ	-40.34	56.18	-3.78	116.84	-14.53
	K_{T_δ}	3.52	64.80	-	-	2.59
	VAF_ϕ	81.15		69.61		80.01
	VAF_δ	93.43		23.34		66.84
	VAF_ψ	93.78		69.67		83.30
3.6 ms^{-1}	K_ϕ	-51.02	56.62	-15.40	55.90	-21.25
	K_δ	2.50	170.45	2.81	50.20	2.79
	K_ϕ	-120.51	85.28	-22.82	102.83	-76.41
	K_δ	16.58	153.27	3.94	243.76	17.14
	K_ψ	-43.06	79.41	-7.37	147.32	-13.30
	K_{T_δ}	3.42	62.79	-	-	3.09
	VAF_ϕ	82.85		79.48		73.14
	VAF_δ	91.63		53.29		52.83
	VAF_ψ	95.10		84.88		71.58
4.7 ms^{-1}	K_ϕ	-51.78	64.60	-19.26	349.70	-14.88
	K_δ	2.75	160.68	4.42	438.96	3.04
	K_ϕ	-136.22	105.15	-27.02	111.78	-48.91
	K_δ	3.21	1156.00	0.01	492609.67	16.01
	K_ψ	-64.43	87.60	-14.29	412.99	-10.82
	K_{T_δ}	3.70	63.91	-	-	2.61
	VAF_ϕ	77.86		71.14		63.73
	VAF_δ	81.63		36.19		15.61
	VAF_ψ	90.32		80.57		55.71
5.7 ms^{-1}	K_ϕ	-38.58	136.91	-19.65	110.85	-10.10
	K_δ	1.13	2085.75	5.42	128.32	3.08
	K_ϕ	-120.59	120.57	-33.34	117.63	-30.95
	K_δ	0.00	3969013.40	0.01	280859.33	18.46
	K_ψ	-60.65	95.03	-19.20	183.00	-8.17
	K_{T_δ}	4.27	191.50	-	-	2.58
	VAF_ϕ	73.65		70.08		49.58
	VAF_δ	77.99		40.64		-
	VAF_ψ	84.32		79.50		39.90

Table 3.4: Results for the VDROP model as estimated for the median rider for all speed levels. Results are presented for the three conditions. Haptic on/off differentiates based on the dynamics of the bicycle model, while "with or w/o T_δ feedback" differentiates based on the structure of the rider control model. The values of the gains are presented as well as their corresponding uncertainty level measured by the coefficient of variation CV_i . Additionally, the variance accounted for of the orientation outputs between parametric and non parametric signals is also presented. The derivative gains ($K_{\dot{\phi}}, K_{\dot{\delta}}$) are measured in $\text{kgm}^2 \text{s}^{-2}$ while the proportional gains (K_ϕ, K_δ, K_ψ) are measured in $\text{kgm}^2 \text{s}^{-1}$. The torque feedback gain K_{T_δ} is dimensionless.

	Bicycle →	Haptics On				Haptics Off	
		Rider →	with T_δ feedback	w/o T_δ feedback	Value	CV (10^{-4})	Value
Forward Speed			Value	CV (10^{-4})	Value	CV (10^{-4})	Value
2.8 ms^{-1}	K_ϕ	-111.62	152.10	-22.44	28.45	-123.53	27.90
	$K_{\dot{\phi}}$	1.80	234.11	2.62	14.59	8.62	35.62
	K_δ	-248.74	151.15	-24.17	84.44	-239.60	18.65
	$K_{\dot{\delta}}$	45.60	150.24	4.05	147.97	22.82	90.52
	K_ψ	-94.18	156.50	-9.03	65.63	-91.07	14.16
	K_{T_δ}	4.66	170.99	-	-	7.93	27.78
	VAF$_\phi$	78.80		82.33		80.67	
	VAF$_\delta$	98.21		68.99		97.59	
	VAF$_\psi$	94.04		90.77		94.95	
3.6 ms^{-1}	K_ϕ	-94.83	125.80	-22.08	33.58	-97.15	115.92
	$K_{\dot{\phi}}$	3.33	404.51	3.34	17.01	9.68	75.60
	K_δ	-249.80	64.02	-37.61	80.02	-249.84	214.29
	$K_{\dot{\delta}}$	58.12	63.15	7.44	140.22	50.23	247.35
	K_ψ	-125.36	97.89	-17.72	66.95	-119.20	160.68
	K_{T_δ}	4.24	91.84	-	-	7.57	95.88
	VAF$_\phi$	81.66		86.50		83.35	
	VAF$_\delta$	97.33		79.27		96.15	
	VAF$_\psi$	96.13		96.97		96.80	
4.7 ms^{-1}	K_ϕ	-120.38	145.55	-27.59	56.00	-164.59	112.31
	$K_{\dot{\phi}}$	0.24	4252.46	4.15	59.72	22.39	106.46
	K_δ	-249.40	133.42	-37.98	90.28	-249.82	107.93
	$K_{\dot{\delta}}$	29.49	210.73	2.67	665.03	14.70	649.60
	K_ψ	-222.31	143.06	-31.24	81.57	-209.12	111.47
	K_{T_δ}	5.75	141.98	-	-	13.87	78.12
	VAF$_\phi$	79.21		81.88		80.97	
	VAF$_\delta$	97.07		70.43		90.44	
	VAF$_\psi$	92.97		95.43		95.93	
5.7 ms^{-1}	K_ϕ	-83.24	24.27	-27.53	46.08	-146.38	35.81
	$K_{\dot{\phi}}$	0.65	1394.64	4.31	43.06	28.45	31.76
	K_δ	-169.81	13.03	-44.71	92.82	-246.85	116.80
	$K_{\dot{\delta}}$	8.29	278.33	4.13	493.77	29.42	401.88
	K_ψ	-185.36	6.72	-43.34	72.02	-211.40	56.88
	K_{T_δ}	4.49	72.85	-	-	15.81	10.28
	VAF$_\phi$	82.35		85.06		80.57	
	VAF$_\delta$	96.12		75.40		87.27	
	VAF$_\psi$	93.83		97.03		93.59	

While the delayed control input of the rider is expected in the variable delay model, a noticeable delay can be discerned even in the ideal zero delay model (see figure 3.10). This occurs because of the lag induced by the neuromuscular transfer function (see equations (3.12) and (3.13)), the parameters of which do not seem to fall in line with the measured behavior as the response of the rider to the disturbance in the non-parametric model is much faster.

Major discrepancies can be discerned in the non-parametric rider torque and the parametric torque for all models in the haptics off with T_δ condition (see figures 3.18 and 3.19). A choice was made to optimize the fit of the haptics off case with the non-parametric data-set of the haptics on condition, so as to make the impact of the change directly comparable. The non-parametric data-set of the haptics off experimental condition could have been used but that would invalidate the purpose of the analysis, which is to see to what extent different torque feedback levels can approximate the same rider response.

While the assumption that steering is the only active control input for the task of bicycle roll stabilization is correct, a secondary task is not taken into account by leaving the upper body unconstrained, which revolves around balancing of the torso and head. As a result, VAF_ϕ never reaches values higher than 85 %. This assumption was confirmed by performing a non linear model simulation, where bicycle and rider were modeled as two inverted pendulums with torsional spring and dampers in the two hinges. It was found that when a controller, that tries to keep the center of mass of the upper pendulum constant, was activated the lean of the lower pendulum got larger compared to the case where both pendulums are rigidly connected. Consequently, the degree to which the rider can extrapolate information from their vestibular system to make deductions on the state of the bicycle is debatable, since the vestibular system measures roll rate and acceleration of the head and not the actual bicycle frame. However since this remains consistent among conditions, the effectiveness of the torque feedback loop will remain analogous.

A conclusion on the importance of T_δ feedback can not be made by looking at the coefficient of variation, however the impact on fitting performance is significant. This is indicated by the fact that when the torque feedback loop is severed VAF_δ drops by at least 15% for all models tested. Even in the variable delay model, torque feedback is potent enough to compensate for the delays and achieve over 90 % fit in steering response for the lower forward speeds (see table 3.3). This could be, because torque inherently includes acceleration information and can give the rider a preview of how the rest of the state is going to evolve. However, in the haptics off condition, where the torque feedback is not physiologically severed but lessened due to the changed steering dynamics, major degradation in fitting performance was only noted for the model with uncompensated time delays. In this case torque feedback is still proportional to the steering acceleration so the "preview" information is not completely lost. However the rider receives no input for the effect of the disturbance because the torque that would naturally transfer through the front wheel contact point is filtered by the uncoupled fork-handlebar connection. Despite all that, in the VDROP model, VAF_δ did not drop more than 8% and VAF_ϕ , VAF_ψ showed an even more insignificant drop, which could explain why no difference was found between steering configurations in the experiments conducted in [5].

The pattern noted by the coefficient of variation of the derivative steering angle gain in the VDROP model indicates that when T_δ feedback is present, the reflexive modulation of steering damping does not contribute to the successful rejection of lateral disturbances (see table 3.4). This was further confirmed by removing the $\dot{\delta}$ feedback loop and noting that the VAF_δ did not drop significantly (< 1%). However without T_δ feedback, it seems that δ feedback becomes the least important for the fit.

The prediction strategy used manages to utilize the smith principle to enhance the optimal predictions of the tapped delay line with information of the effect of the disturbance on the state through reafferent pathways and simultaneously compensate for internal model inaccuracies. Note that in the haptics off case the internal mode was not updated to reflect the changed dynamics, but the predictor manages to filter out the small discrepancies by comparing the forward model output with the delayed state measurements.

Given the above findings regarding the importance of torque feedback the VDROP model with T_δ feedback in the haptics on configuration was tested against a validation dataset to ensure its prediction capability for a different set of measurements. By taking into consideration the level of inter subject variability that is present in all human related tasks the results are more than acceptable (see table 3.1).

3.5. CONCLUSIONS

In an effort to iterate over existing rider control models, the VDROP model is created that successfully accounts for sensory delays by the use of an internal forward model. It is shown that implementation of delay without some compensation does not produce results that match the experimental data. A prediction strategy is developed that manages to circumvent the inability of the conventional smith predictor to work on inherently unstable open loop systems by implementing a resetting forward model (DOP). The results matched the measured non-parametric outputs with a good level of fit. Additionally, the model is found to be robust towards internal model inaccuracies.

Furthermore the importance of the sensory inflow from the golgi tendon organs was thoroughly examined. From the results it is therefore concluded that a proper rider control model should include the torque feedback pathway. Contrary to what the results of the analysis done by Dialynas et al. [5] indicated, this work suggests that torque feedback is in fact crucial to the execution of the balancing task. However the torque feedback in the experiments was not physiologically neutered and state information could be deduced by the remaining inertial properties of the handlebar. Even though a steer-by-wire system decouples the roll and steer dynamics the remaining inertial feedback of the handlebar components (haptics off) was proven to be adequate for the rider to achieve comparable performance between conditions. Further, experiments with negative stiffness applied at the handlebars could be conducted to cancel out inertial steering effects to validate experimentally these results.

Table 3.5: Whipple model parameters for the steer-by-wire bicycle shown in figure 3.2.

Parameter	Symbol	Value
wheel base	w	1.03m
trail	c	0.0665m
steer axis tilt ($\pi/2 - \text{head angle}$)	λ	$\pi/10$
rear wheel	R	
radius	r_R	0.6858m
mass	m_R	8.5 kg
mass moment of inertia	$(I_{R_{xx}}, I_{R_{yy}})$	(0.095625, 0.19125) kg m ²
rear body and frame assembly	B	
position centre of mass	(x_B, z_B)	(0.4, -0.6)
mass	m_B	95kg
mass moment of inertia	$\begin{bmatrix} I_{B_{xx}} & 0 & I_{B_{xz}} \\ 0 & I_{B_{yy}} & 0 \\ I_{B_{xz}} & 0 & I_{B_{zz}} \end{bmatrix}$	$\begin{bmatrix} 9.2 & 0 & 2.4 \\ 0 & 11 & 0 \\ 2.4 & 0 & 2.8 \end{bmatrix}$ kg m ²
front handlebar and fork assembly	H	
position centre of mass	(x_H, z_H)	(0.9, -0.66)
mass	m_H	1.5kg
mass moment of inertia	$\begin{bmatrix} I_{H_{xx}} & 0 & I_{H_{xz}} \\ 0 & I_{H_{yy}} & 0 \\ I_{H_{xz}} & 0 & I_{H_{zz}} \end{bmatrix}$	$\begin{bmatrix} 0.05892 & 0 & -0.00756 \\ 0 & 0.06 & 0 \\ -0.00756 & 0 & 0.00708 \end{bmatrix}$ kg m ²
front wheel	F	
radius	r_F	0.6858m
mass	m_F	1.84kg
mass moment of inertia	$(I_{F_{xx}}, I_{F_{yy}})$	(0.096, 0.195)kg m ²
battery rack	b	
position centre of mass	(x_b, z_b)	(0.4, -0.55)
mass	m_b	4kg
mass moment of inertia	$\begin{bmatrix} I_{H_{xx}} & 0 & I_{H_{xz}} \\ 0 & I_{H_{yy}} & 0 \\ I_{H_{xz}} & 0 & I_{H_{zz}} \end{bmatrix}$	$\begin{bmatrix} 0.02 & 0 & -0.02 \\ 0 & 0.04 & 0 \\ -0.02 & 0 & 0.02 \end{bmatrix}$ kg m ²

Table 3.6: Mass, damping and stiffness matrices for the bicycle model from figure 3.2 according to the parameters from table 3.5. Haptics On refers to the bicycle model used that is subject to the normal bicycle dynamics while Haptics off refers to the model parameters with the decoupled steering dynamics.

Haptics On

$$\mathbf{M}_0 = \begin{bmatrix} 129.560969317222 & 1.90339264112109 \\ 1.90339264112109 & 0.153300561290599 \end{bmatrix}, \quad \mathbf{C}_1 = \begin{bmatrix} 0 & 37.686356977648515 \\ -0.540721349837341 & 1.003016812829302 \end{bmatrix}$$

$$\mathbf{K}_0 = \begin{bmatrix} -104.1937454016045 & -1.7093813017294 \\ -1.7093813017294 & -0.4997649614618 \end{bmatrix}, \quad \mathbf{K}_2 = \begin{bmatrix} 0 & 97.758506542423220 \\ 0 & 1.724635288121681 \end{bmatrix}$$

$c_s = 0.014408, \quad l_g = 0.84$

Haptics Off

$$\mathbf{M}_0 = \begin{bmatrix} 129.560969317222 & 1.90339264112109 \\ 0 & 0.096 \end{bmatrix}, \quad \mathbf{C}_1 = \begin{bmatrix} 0 & 37.686356977648515 \\ 0 & 0 \end{bmatrix}$$

$$\mathbf{K}_0 = \begin{bmatrix} -104.1937454016045 & -1.7093813017294 \\ 0 & 0 \end{bmatrix}, \quad \mathbf{K}_2 = \begin{bmatrix} 0 & 97.758506542423220 \\ 0 & 0 \end{bmatrix}$$

$c_s = 0, \quad l_g = 0.84$

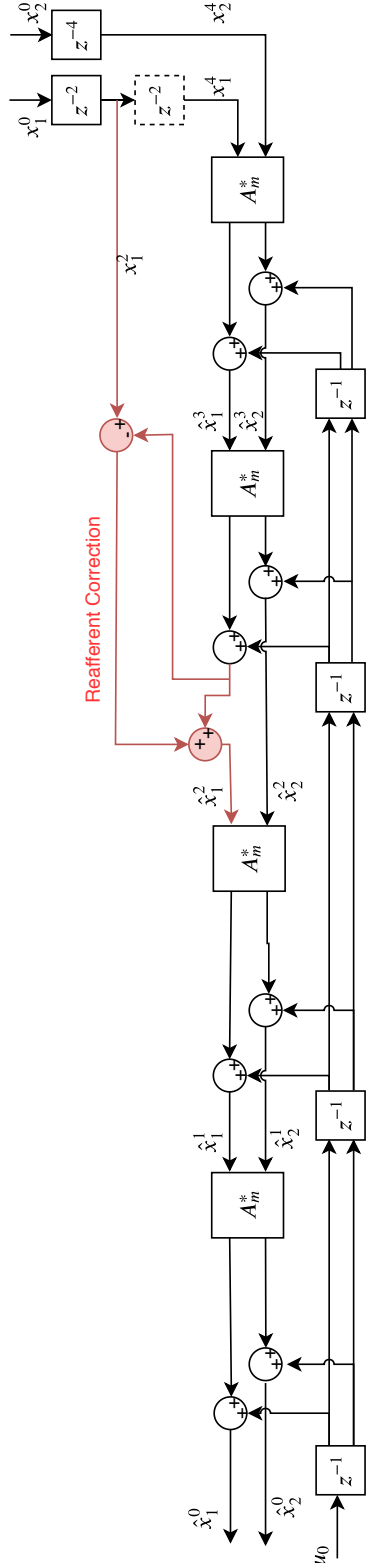


Figure 3.7: Example that illustrates the adaptation necessary for the DOP to work with variable delay signals. States x_1, x_2 are delayed according to their individual dead times. Since x_1 has smaller delay value, it is further delayed through a model of the remaining delay to synchronize with x_2 . The delayed state vector enters the tapped delay line until the point when the forward simulation produces an estimate of x_1 that is concurrent with its measurement; in this case after 2 time steps. At that point the reaferent correction is performed shown in red. After the correction the tapped delay line continues normally. Matrices A_m^* and B_m^* are the best available discrete approximation of the system dynamics, u_0 is the current control input (eference copy).

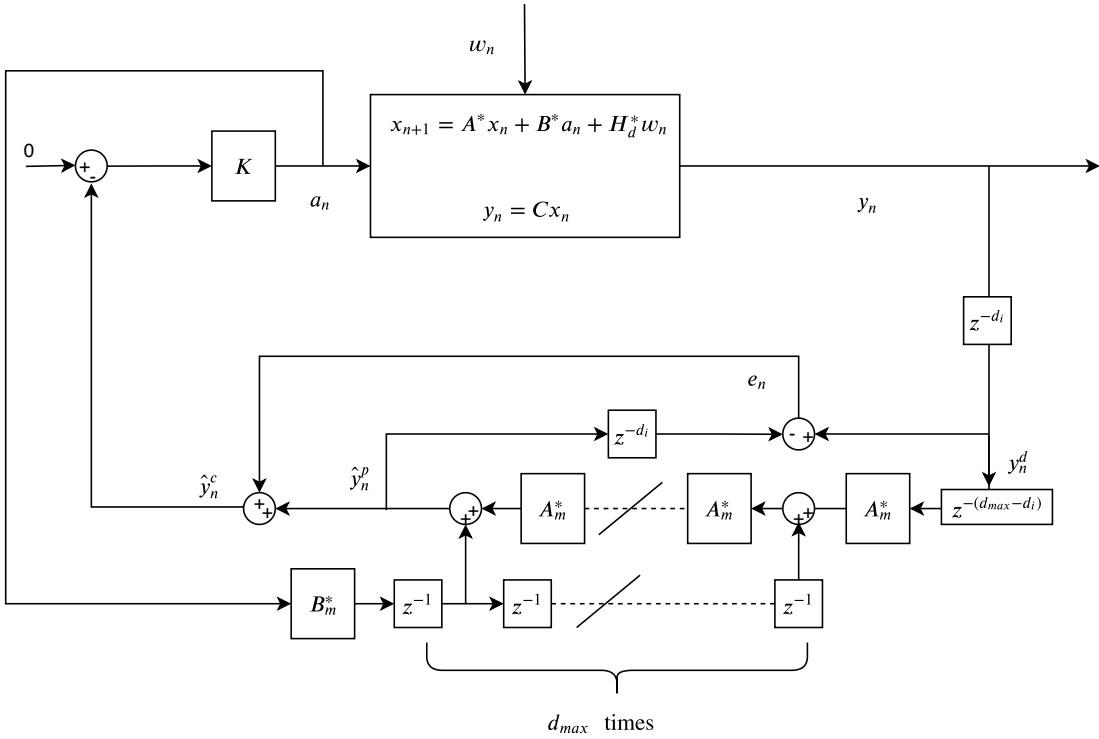


Figure 3.8: Block diagram of the Reafferent Optimal Prediction Model. A^*, B^*, H_d^* are the discretized matrices of the combined plant dynamics, d_i is the amount of delay in time steps per sensory channel and d_{max} the maximum value of those. Matrices A_m^*, B_m^* express the dynamics of the internal model of the process. When the internal model is assumed to be perfect $A_m^* = A^*$ and $B_m^* = B^*$. First the delayed measurements are all further delayed upto the maximum amount of delay among signals in order to synchronize them. The delayed output measurement is forwarded in time (d_{max} times) in the tapped delay line to produce the first undelayed estimate of the output \hat{y}^p . When a less delayed measurement of a certain state becomes available the tapped delay line state register is updated with that measurement. This way the accumulation of forward simulation error is minimized. Output \hat{y}^p is again delayed through a model of the internal time delay. The difference between this re-delayed prediction with the delayed measurements creates the error e which is added back to \hat{y}^p to create the final corrected prediction \hat{y}^c .

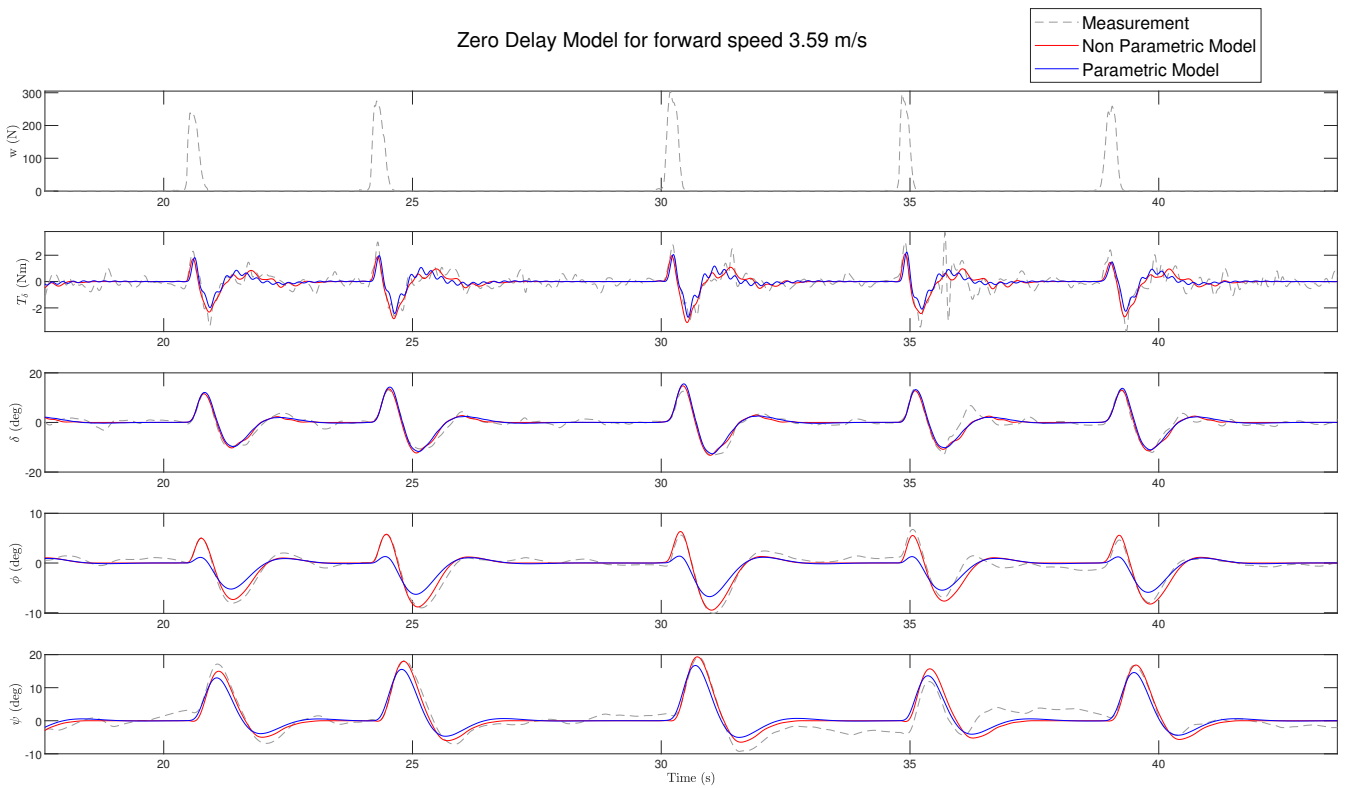
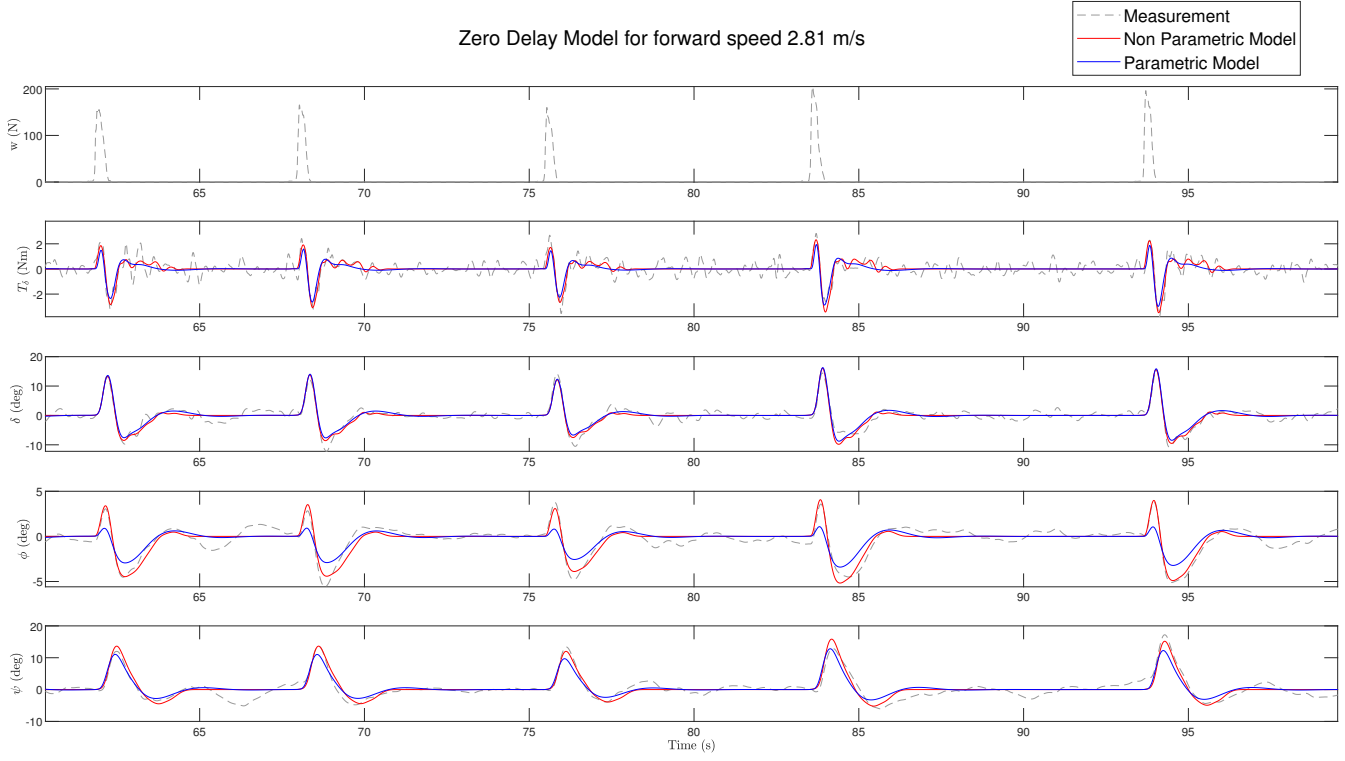
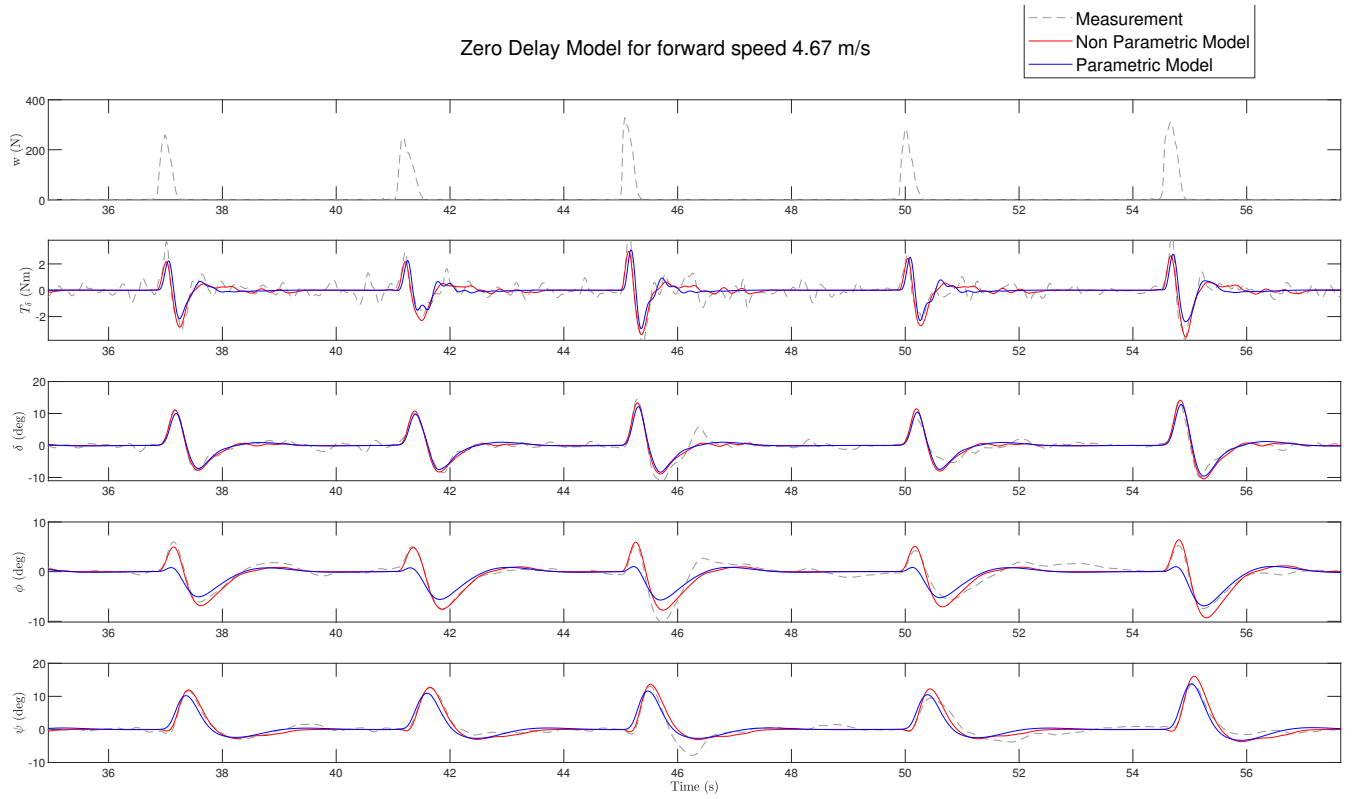
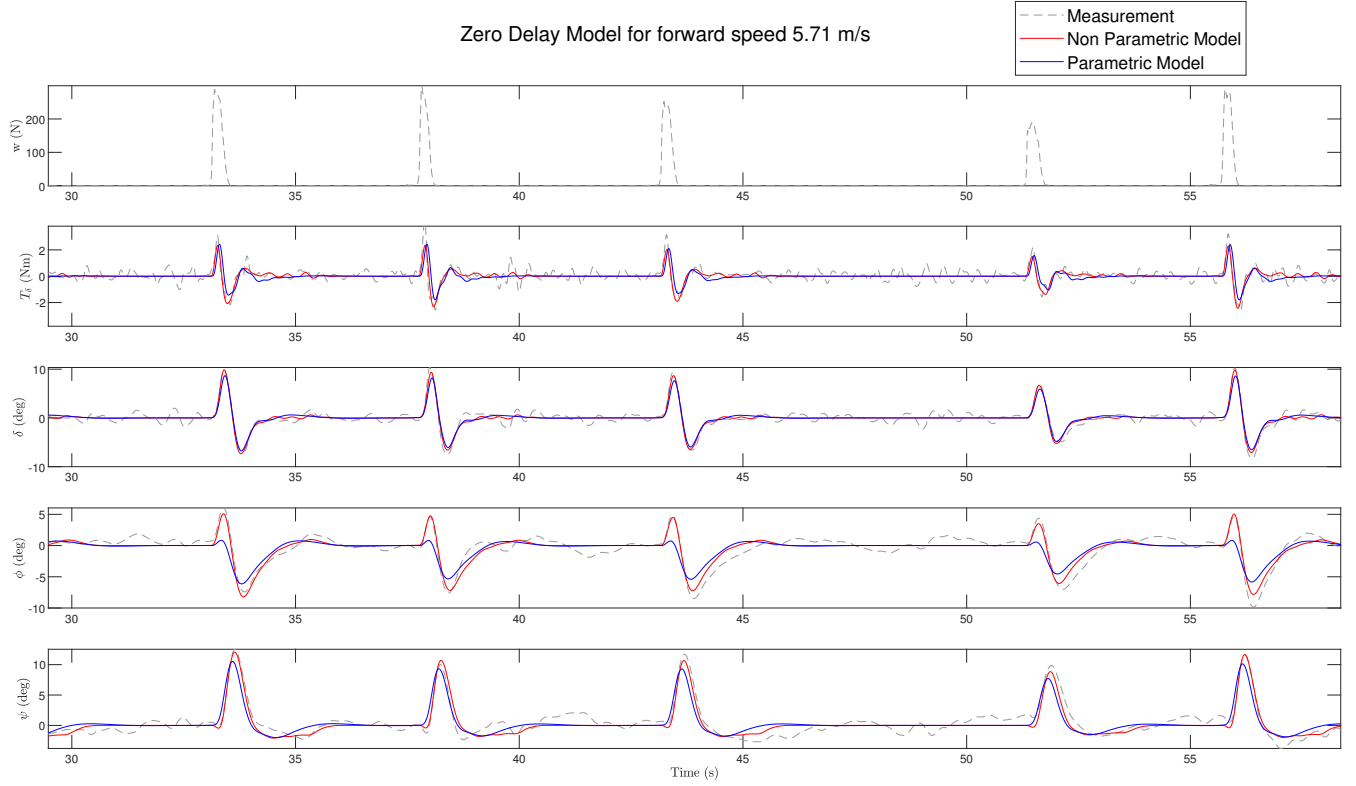


Figure 3.9: Comparison between parametric model output (Zero Delay Model), non-parametric model output and measured signals for the two lowest speed levels for the case where torque feedback is present in the rider control model and bicycle is operating under the "haptics on" dynamics.



(a)



(b)

Figure 3.10: Comparison between parametric model output (Zero Delay Model), non-parametric model output and measured signals for the two highest speed levels for the case where torque feedback is present in the rider control model and bicycle is operating under the "haptics on" dynamics.

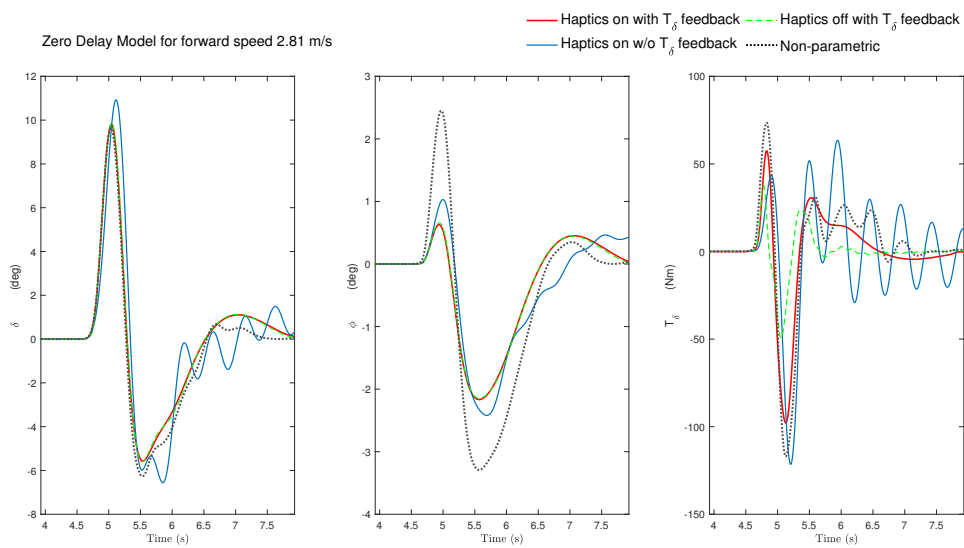
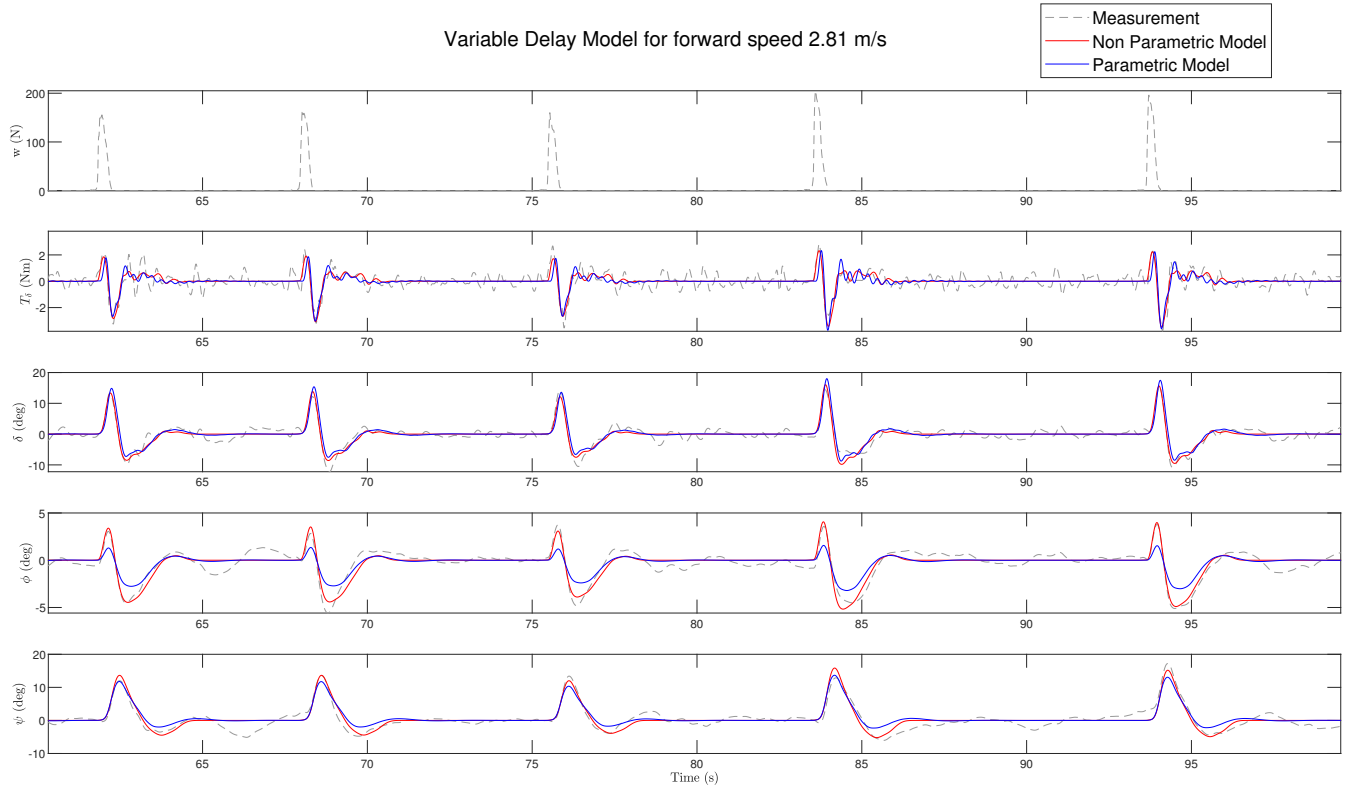
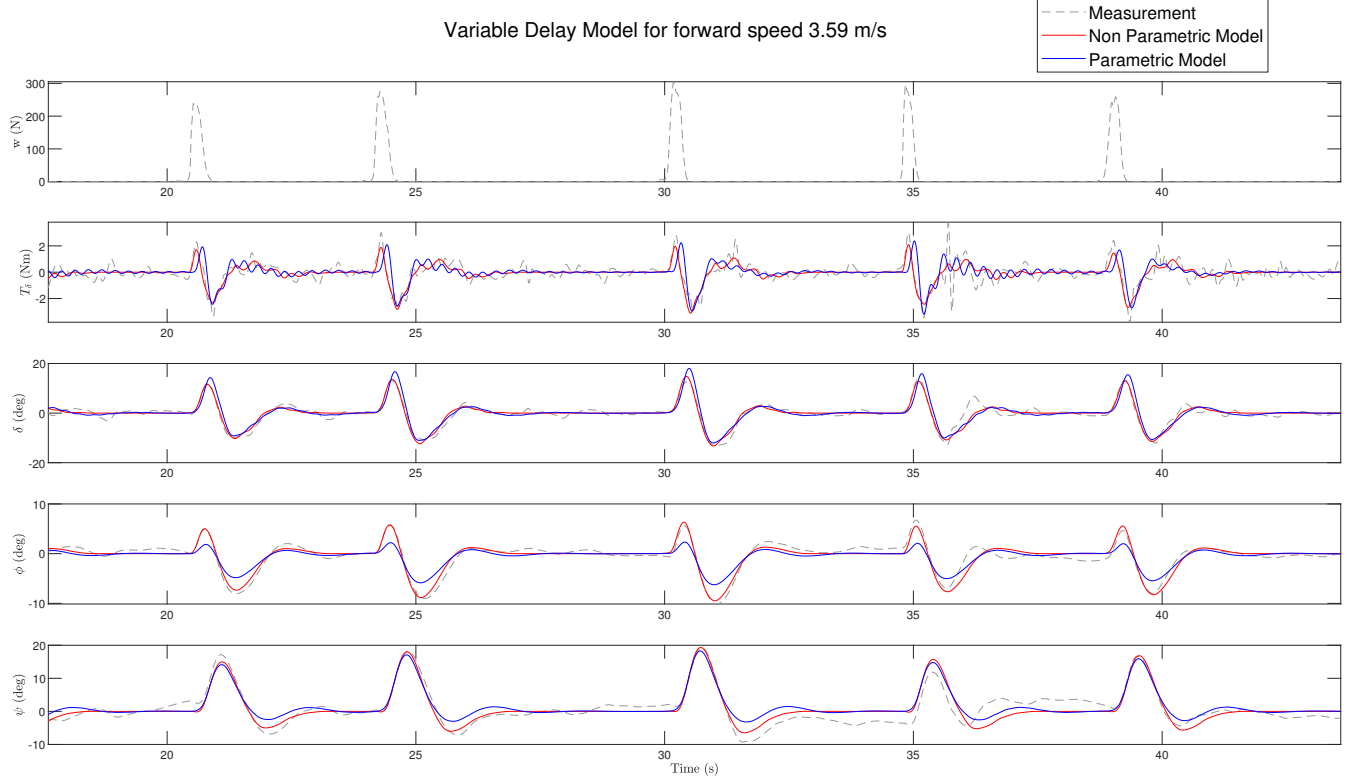


Figure 3.11: Steering, roll angles and input rider torque compared among torque feedback levels for the forward speed of 2.81 ms^{-1} in the Zero Delay Model. Response of the first disturbance in the run is shown.

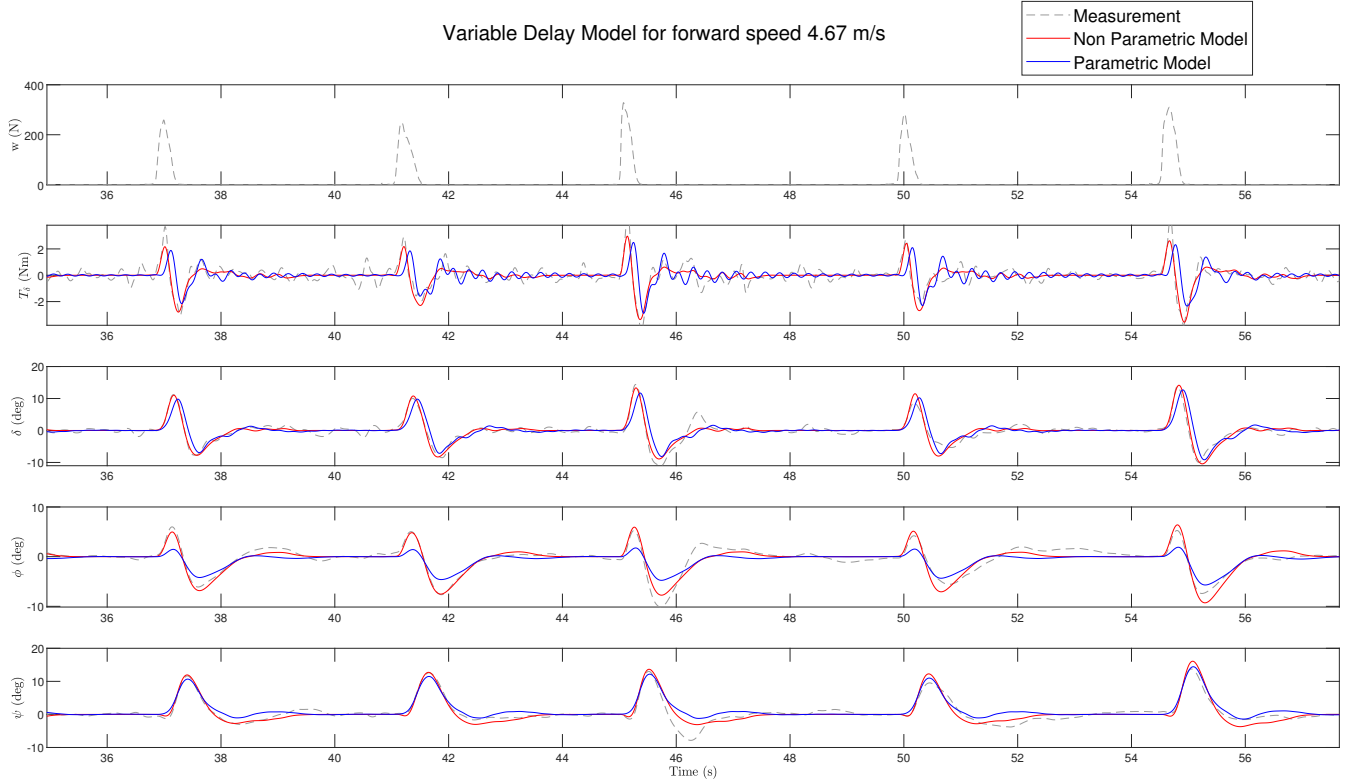


(a)

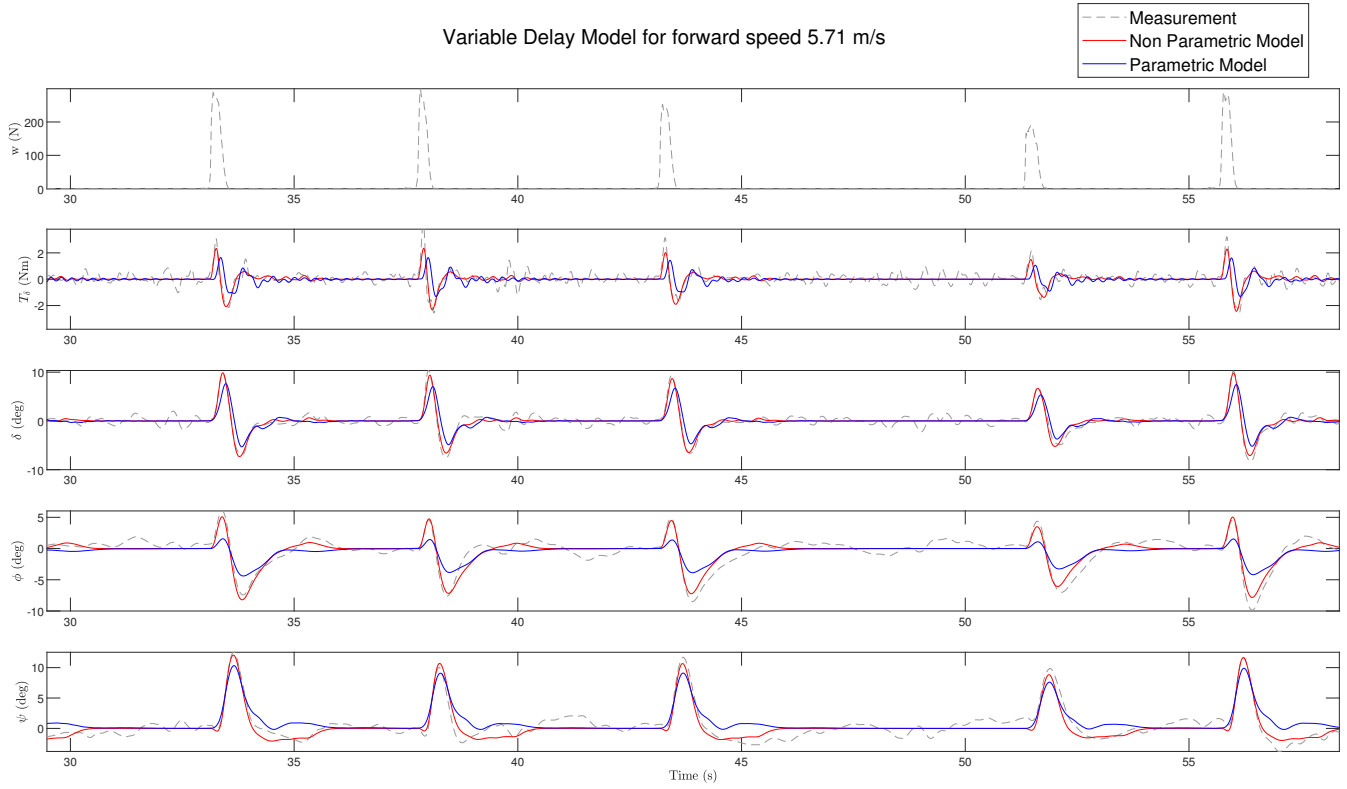


(b)

Figure 3.12: Comparison between parametric model output (Variable Delay Model), non-parametric model output and measured signals for the two lowest speed levels for the case where torque feedback is present in the rider control model and bicycle is operating under the "haptics on" dynamics.



(a)



(b)

Figure 3.13: Comparison between parametric model output (Variable Delay Model), non-parametric model output and measured signals for the two highest speed levels for the case where torque feedback is present in the rider control model and biccyle is operating under the "haptics on" dynamics.

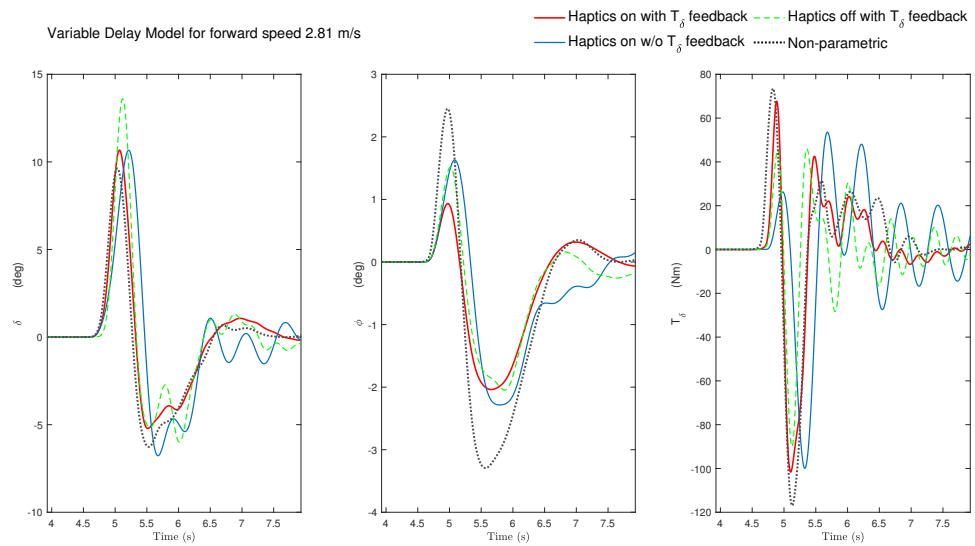
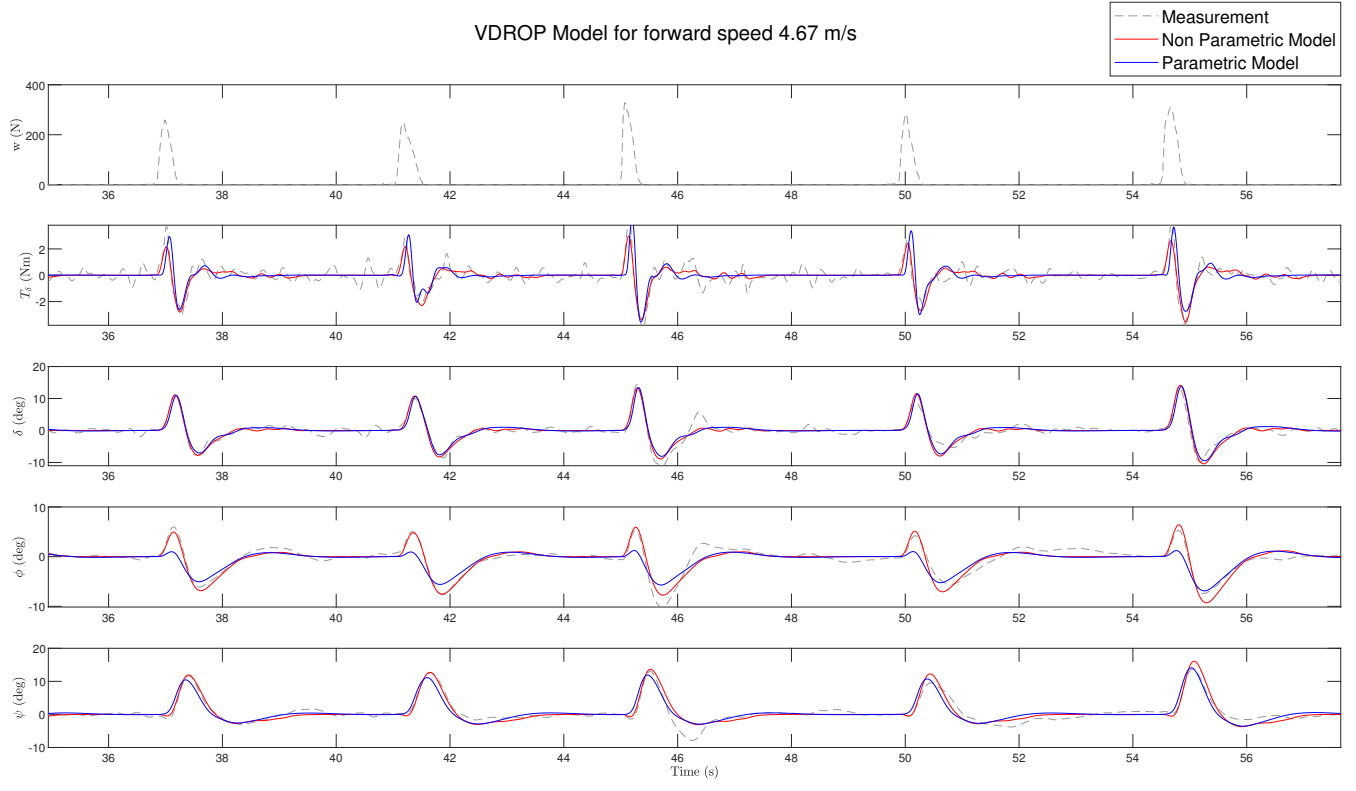


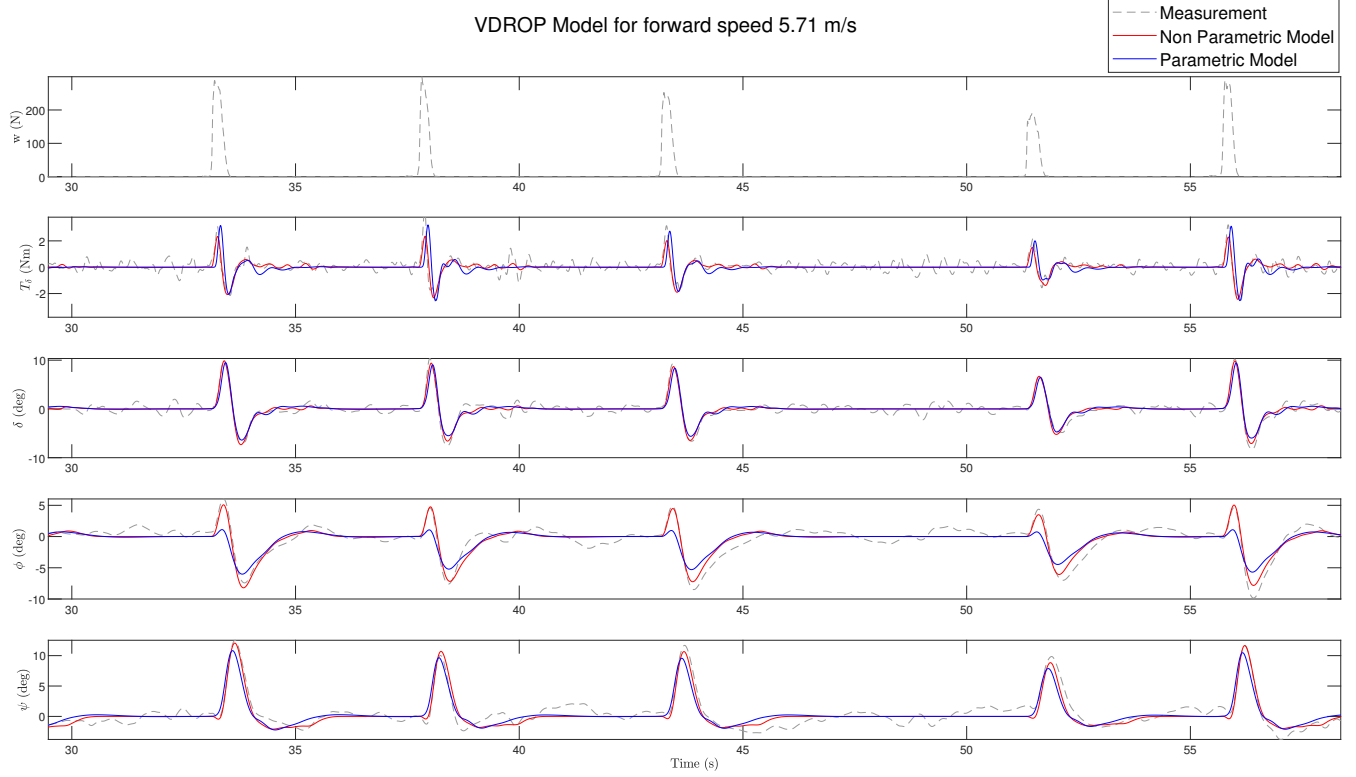
Figure 3.14: Steering, roll angle and input rider torque of the median rider compared among torque feedback levels for the forward speed of 2.81 m s^{-1} in the Variable Delay Model. Response of the first disturbance in the run is shown.



Figure 3.15: Comparison between parametric model output (VDROP Model), non-parametric model output and measured signals for the two lowest speed levels for the case where torque feedback is present in the rider control model and bicycle is operating under the "haptics on" dynamics.



(a)



(b)

Figure 3.16: Comparison between parametric model output (VDROP Model), non-parametric model output and measured signals for the two highest speed levels for the case where torque feedback is present in the rider control model and bicycle is operating under the "haptics on" dynamics.

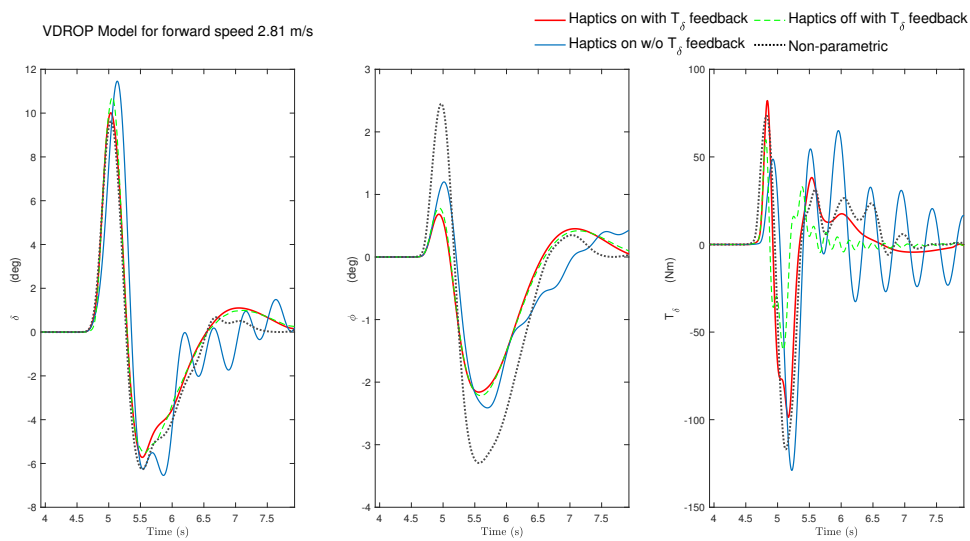


Figure 3.17: Steering, roll angles and input rider torque compared among torque feedback levels for the forward speed of 2.81 m s^{-1} in the VDROP Model. Response of the first disturbance in the run is shown.

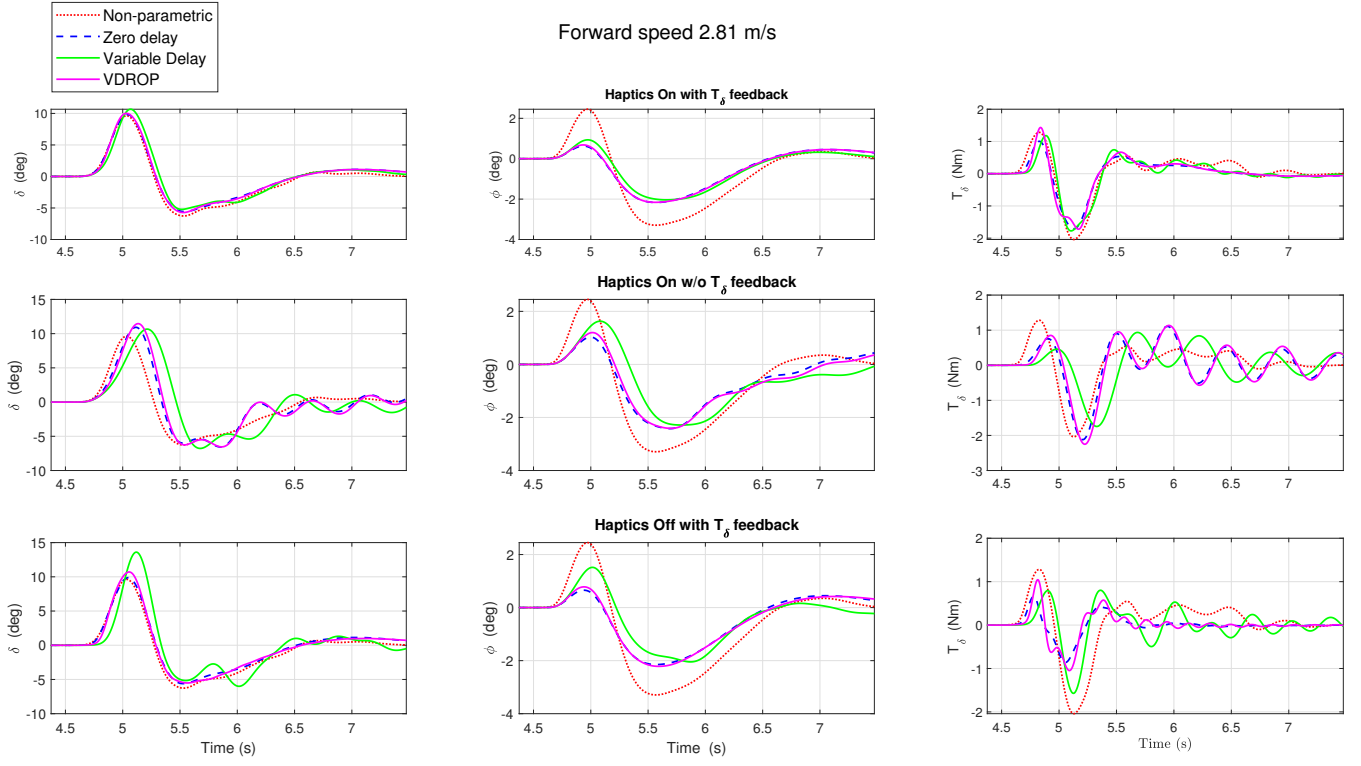
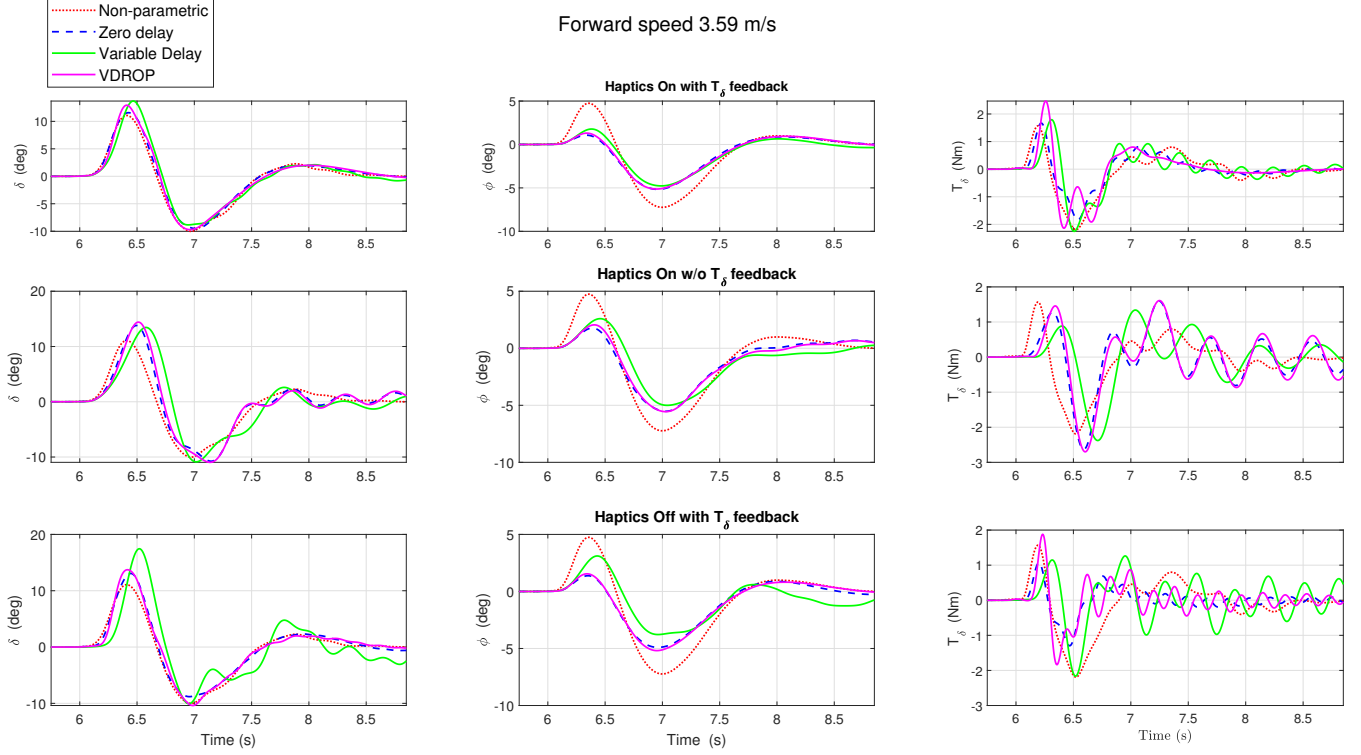
(a) Comparison between the three rider models for forward speed 2.81 ms^{-1} (b) Comparison between the three rider models for forward speed 3.6 ms^{-1}

Figure 3.18: Steering angle δ , roll angle ϕ and steering torque T_δ compared among the three rider models implemented for all torque feedback conditions, for the two lowest speed levels for the response of the median rider to the first perturbation of each run. Non parametric output included for reference.

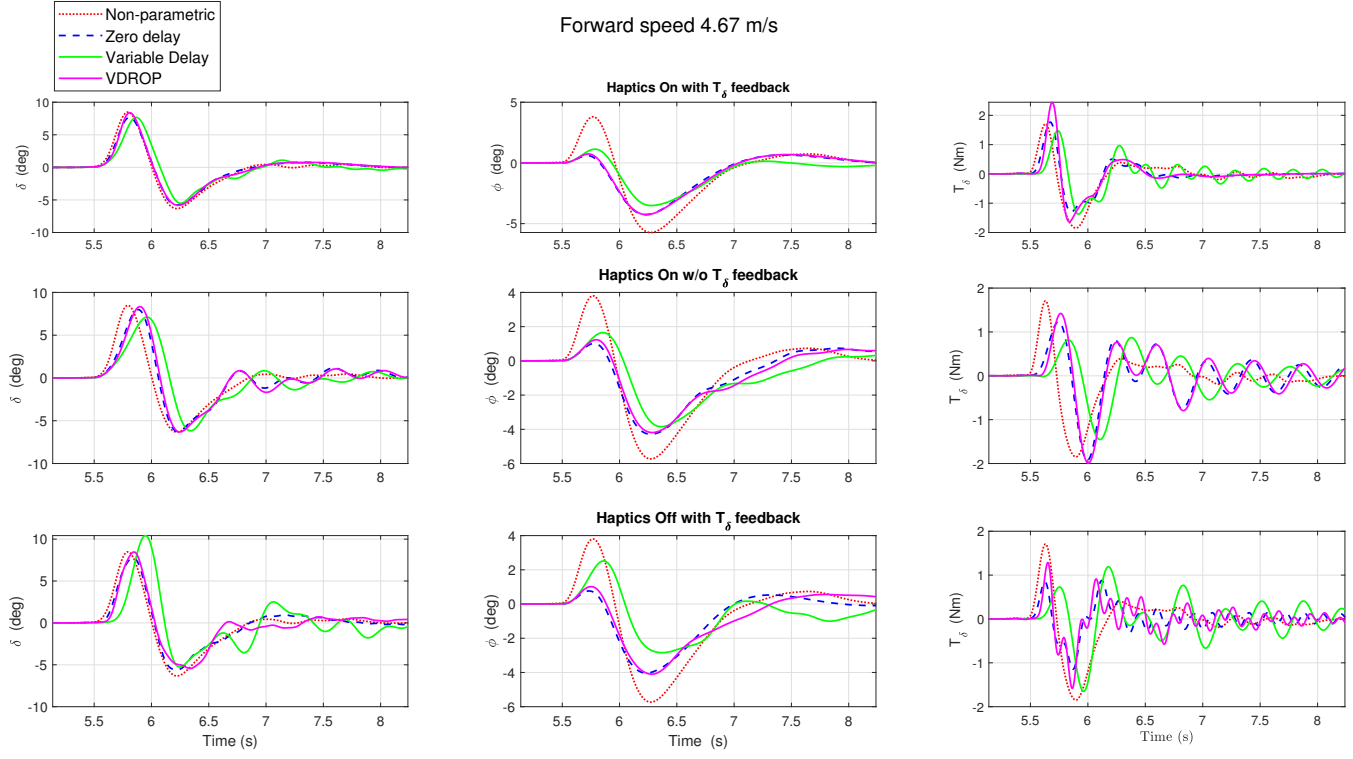
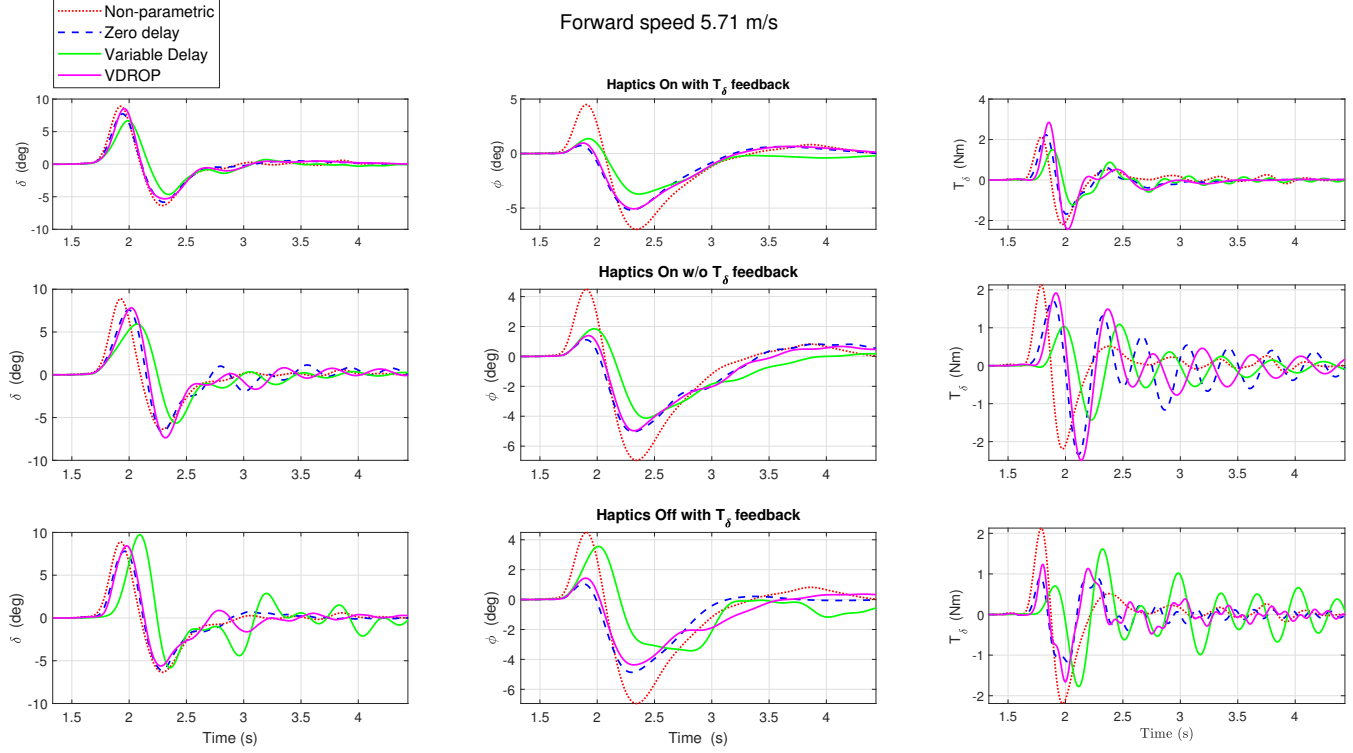
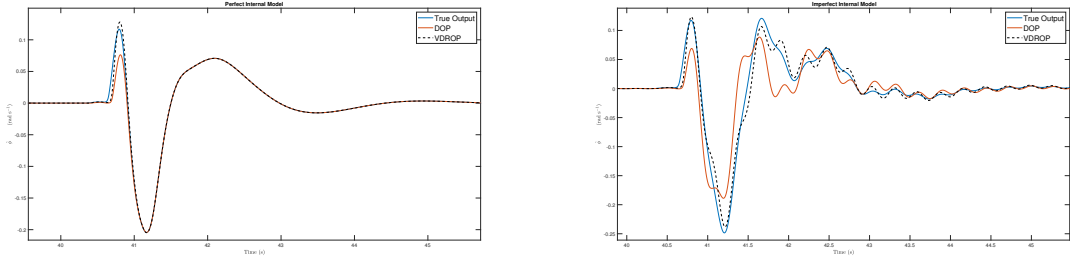
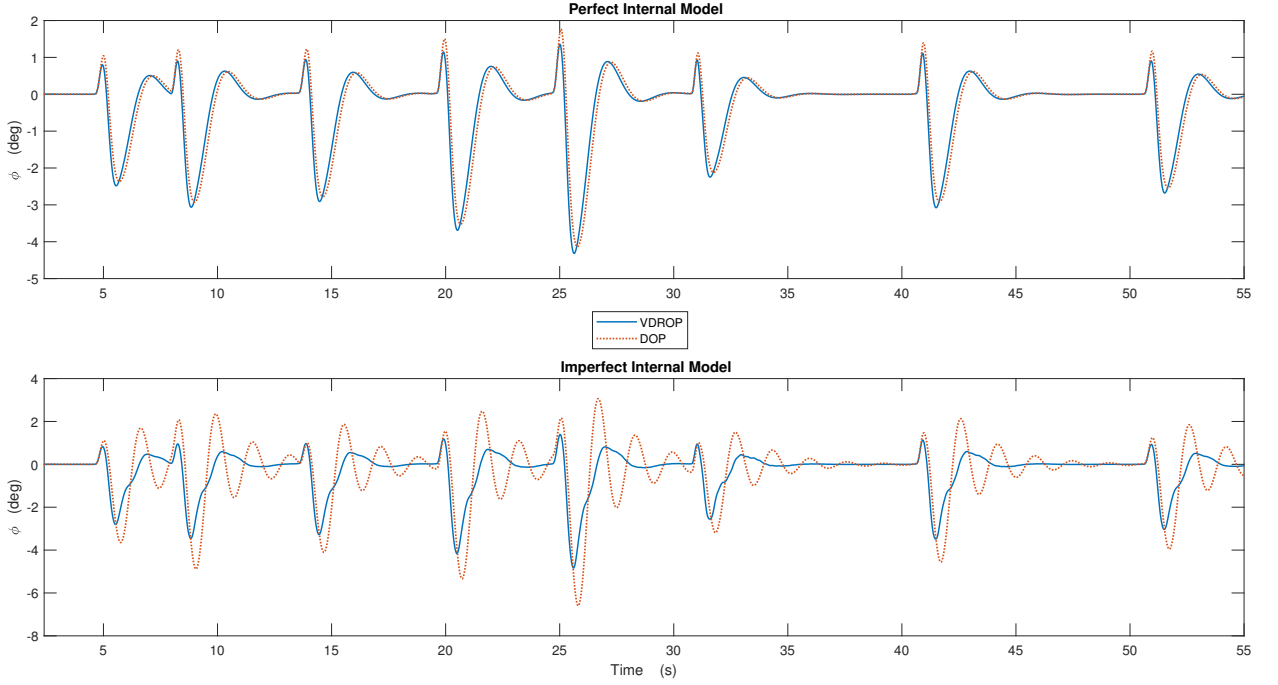
(a) Comparison between the three rider models for forward speed 4.67 ms^{-1} (b) Comparison between the three rider models for forward speed 5.71 ms^{-1}

Figure 3.19: Steering angle δ , roll angle ϕ and steering torque T_δ compared among the three rider models implemented for all torque feedback conditions, for the two highest speed levels for the response of the median rider to the first perturbation of each run. Non-parametric output included for reference.



(a) Comparison between true roll rate, and predicted roll rate using the Variant Delay optimal Predictor (VDROP) and the Discrete Optimal Predictor (DOP). In the left graph a perfect internal model is used while in the right graph imperfections are introduced.



(b) Roll angle ϕ compared between the Variant Delay optimal Predictor and the Discrete Optimal Predictor . In the top graph a perfect internal model is used while in the bottom graph imperfections are introduced.

Figure 3.20: Results of the simulation using imperfect internal model. In (a) the state estimate of the roll rate is compared among prediction algorithms, while in (b) the roll stabilization response to a prolong run subject to the different prediction strategies is shown.

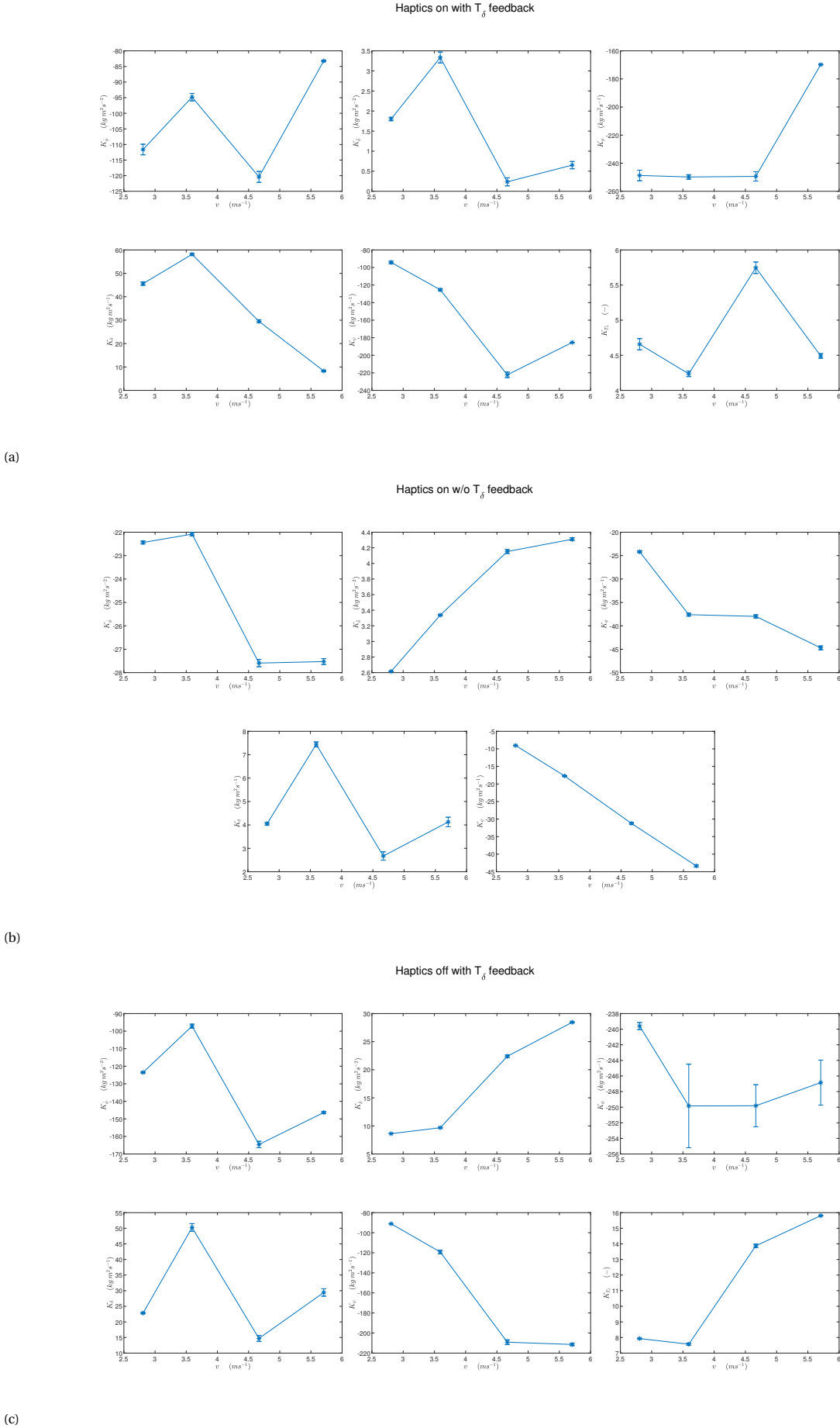


Figure 3.21: Feedback control gains (K) as a function of forward velocity (v) for the different torque feedback levels for the median rider in the VDROP Model. Error bars indicate the standard error of the mean calculated from the covariance matrix calculated by equation (3.16).

A

CALIBRATION OF INERTIAL MEASUREMENTS

The fixed body angular velocities measured by the Inertial Measurement Unit (IMU) are biased due the imperfect orientation of the sensor axis (see figure A.1). The goal is it to align system xyz with the global coordinate system XYZ. To achieve this the euler angle offsets are calculated by using the measurements from MPU-9050's built in accelerometer.



Figure A.1: Bicycle with body fixed sensor axis x-y-z (B) and global axis XYZ (G).

Different orders of rotation affects the end configuration. For this study the intrinsic order Z-Y'-X'' is adopted which is equivalent to the extrinsic X-Y-Z (roll-pitch-yaw). The inverse rotation matrix that described the above rotation sequence is :

$$R_{xyz} = R_x(\phi)R_y(\theta)R_z(\psi) = \begin{pmatrix} \cos\theta \cos\psi & \cos\theta \sin\psi & -\sin\theta \\ \cos\psi \sin\theta \sin\phi - \cos\phi \sin\psi & \cos\phi \cos\psi + \sin\theta \sin\phi \sin\psi & \cos\theta \sin\phi \\ \cos\phi \cos\psi \sin\theta + \sin\phi \sin\psi & \cos\phi \sin\theta \sin\psi - \cos\psi \sin\phi & \cos\theta \cos\phi \end{pmatrix} \quad (\text{A.1})$$

(a) Configuration $i = 1$ (b) Configuration $i = 2$

Figure A.2: a) The bicycle's desired Z axis is aligned with the vector of gravitational acceleration. The bike was validated to be completely upright by the use of a calibrated commercial IMU (MTw Awinda). b) The bicycle's desired X axis is aligned with the vector of gravitational acceleration. The door was validated to be completely vertical by the use of a calibrated commercial IMU (MTw Awinda). \mathbf{g} is the vector measured by the accelerometer which opposite to the gravitational acceleration.

where ϕ is the angle of rotation around axis X, θ is the angle of rotation around axis Y and ψ is the angle of rotation around axis Z. Equation (A.1) maps a vector from the global system G to the body fixed system B. In order to estimate the euler angle offsets the bike was configured in two different ways to align the gravity vector with the z and x axis respectively. The readings from the accelerometer are expressed in the sensor frame (B). Equation (A.2) is used to solve for the euler angle offsets. Unfortunately the three equations have only two degrees of freedom so two configurations are required so as to solve for all three angles.

In the first, $i = 1$ and $\mathbf{g}_1 = [0 \ 0 \ 1]^T$ (see figure A.2a) (note that the vector of accelerations is normalized) with equation (A.2) solving for θ and ϕ . The lack of any dependence on the yaw angle is intuitive to understand since a rotation around the z-axis is aligned with the gravitational field and accelerometers are completely insensitive to rotations about the gravitational field vector. Consequently in the second, $i = 2$ and $\mathbf{g}_2 = [-1 \ 0 \ 0]^T$ which leads to equation (A.2) solving for ψ and θ (see figure A.2b).

$$\frac{\mathbf{G}_i^B}{\|\mathbf{G}_i^B\|} = \begin{pmatrix} G_{ix}^B \\ G_{iy}^B \\ G_{iz}^B \end{pmatrix} \frac{1}{\sqrt{G_{ix}^{B^2} + G_{iy}^{B^2} + G_{iz}^{B^2}}} = \mathbf{R}_{xyz(\phi_o, \theta_o, \psi_o)} \mathbf{g}_i \quad (\text{A.2})$$

Solving equation (A.2) for the angles we get :

$$\phi_o = \tan^{-1} \left(\frac{G_{1y}^B}{G_{1z}^B} \right) \quad (\text{A.3})$$

$$\theta_o = \tan^{-1} \left(\frac{G_{1x}^B}{\sqrt{G_{1y}^B{}^2 + G_{1z}^B{}^2}} \right) \quad (\text{A.4})$$

$$\psi_o = \tan^{-1} \left(\frac{-G_{2y}^B}{\sqrt{G_{2x}^B{}^2 + G_{2z}^B{}^2}} \right) \quad (\text{A.5})$$

From equations (A.3) to (A.5) the euler angle offsets calculated are inserted into rotation matrix R_{xyz} . The transpose of the result (A.6) is then used to transform the IMU measurements from the coordinate frame B to the coordinate frame G which is consistent with the linearized equations of motion defined in ??.

$$R_{IMU} = R_{xyz}^T(\phi_o, \theta_o, \psi_o) = \begin{pmatrix} 0.9939 & -0.006106 & -0.1105 \\ 0.006069 & 1.0 & -0.000675 \\ 0.1105 & 0 & 0.9939 \end{pmatrix} \quad (\text{A.6})$$

B

ORIENTATION ESTIMATION FROM INERTIAL MEASUREMENTS

In order to properly assess the state of the bicycle when comparing it with the Whipple model, measurements of roll angle ϕ and yaw angle ψ are necessary. However the steer-by-wire bicycle has no way of measuring either. For this reason an estimation method is required that can approximate these angles by using measurements from already existing Inertial sensors. A distinction is made between methods that can estimate the euler angles when the whole signal is available for processing and for methods that can produce real-time estimation.

B.1. OFFLINE ESTIMATION METHODS

An estimation of the roll and yaw angle can be made by using the angular rates measured by the gyroscope. However euler angle rates and angular velocities are not equivalent as the former are dependant on order of rotation while the latter are a vector expressed in the body frame. For this reason an expression needs to be formulated that connects the two. Since the euler angle rates are expressed in the local frame of that particular rotation sequence, appropriate rotation matrices need to be used to transform them into vectors in the final body fixed frame (B). The order of rotation used here is the intrinsic X-Y'-Z" (roll-pitch-yaw).

$$\begin{pmatrix} {}^B\omega_x \\ {}^B\omega_y \\ {}^B\omega_z \end{pmatrix} = \begin{pmatrix} 0 \\ 0 \\ \psi \end{pmatrix} + {}^B R_G \begin{pmatrix} 0 \\ \dot{\theta} \\ 0 \end{pmatrix} + {}^B R_G {}^G R_F \begin{pmatrix} \dot{\phi} \\ 0 \\ 0 \end{pmatrix} \quad (\text{B.1})$$

where ${}^B\omega_x, {}^B\omega_y, {}^B\omega_z$ the angular rates measured by the gyroscope and F, G the local coordinate systems after the first and second rotation respectively. Note that these measurements are corrected for the imperfect orientation of the IMU sensor by transforming with matrix R_{IMU} (see equation (A.6))

$$\begin{pmatrix} {}^B\omega_x \\ {}^B\omega_y \\ {}^B\omega_z \end{pmatrix} = \begin{pmatrix} 1 & 0 & -\sin\theta \\ 0 & \cos\phi & \cos\theta \sin\phi \\ 0 & -\sin\phi & \cos\phi \cos\theta \end{pmatrix} \begin{pmatrix} \dot{\phi} \\ \dot{\theta} \\ \dot{\psi} \end{pmatrix} \quad (\text{B.2})$$

Simply solving equation (B.2) for the euler angle rates yields the expressions that can be used to calculate the roll and yaw rates from gyroscope measurements.

$$\dot{\phi} = ({}^B\omega_y \sin\phi + {}^B\omega_z \cos\phi) \tan\theta + {}^B\omega_x \approx {}^B\omega_x \quad (\text{B.3})$$

$$\dot{\psi} = \frac{{}^B\omega_y \sin\phi + {}^B\omega_z \cos\phi}{\cos\theta} \approx {}^B\omega_y \sin\phi + {}^B\omega_z \cos\phi \quad (\text{B.4})$$

The newly calculated euler angle rate signals can now be numerically integrated to produce the corresponding euler angles. However, a way needs to be found to account for the accumulating integration error. When the whole signal is available, which is true only in offline (post-processing) applications, two methods were tested for approximating euler angles. The first method removes the drift simply through the use of a high-pass filter. All frequency content under 0.05 Hz is filtered. The second method, removes the drift by subtracting the resulting line from a linear regression. Worth noting here that for the yaw angle this will produce good approximations only when the median of the true signal is around zero, which was mostly true since the subjects tried to keep straight heading in order to avoid falling outside the boundaries of the bicycle lane. For the roll angle this assumptions is confidently made since the signal is expected to be centered around zero. The disadvantage of the high-pass filter was that magnitudes of signals are slightly attenuated, while the disadvantage of the linear regression detrending is that a bias can be introduced if the median is not zero.

B.2. ONLINE ESTIMATION METHODS

With no prior knowledge of the resulting drift another method needs to be found to correct the integration output. Fortunately there are existing ways with which two unreliable sources of a signal can be combined in order to produce a more reliable one. For this a secondary source of pseudo measurements is needed.

My first naive implementation was to calculate the roll from the accelerometer data by assuming that gravity is the only force captured in the accelerometer readings. The formulation of the estimators is identical to the equation (A.3). However, this is not ideal for the particular application of single track vehicles since lateral accelerations due to centrifugal forces heavily change the accelerometer measurements.

Sanjurjo et al. [31] used equations B.5 and B.6 as pseudo absolute measurements. Note that B.6 is directly derived from the second equation of B.2. They explain that equation B.5 is more reliable for angles close to zero and equation B.6 is more reliable for larger roll angles, for this reason a weighted sum of the two methods is employed B.7 that follows the weighting function B.8 .

$$\phi_d = \tan^{-1} \left(\frac{\omega_z^B v}{g} \right) \quad (\text{B.5})$$

$$\phi_\omega = \tan^{-1} \left(\frac{\omega_y^B}{\omega_z^B} \right) \quad (\text{B.6})$$

$$\phi_m = W\phi_d + (1 - W)\phi_\omega \quad (\text{B.7})$$

$$W = \exp \left(-\frac{\hat{\phi}^2}{\bar{\phi}^2} \right) \quad (\text{B.8})$$

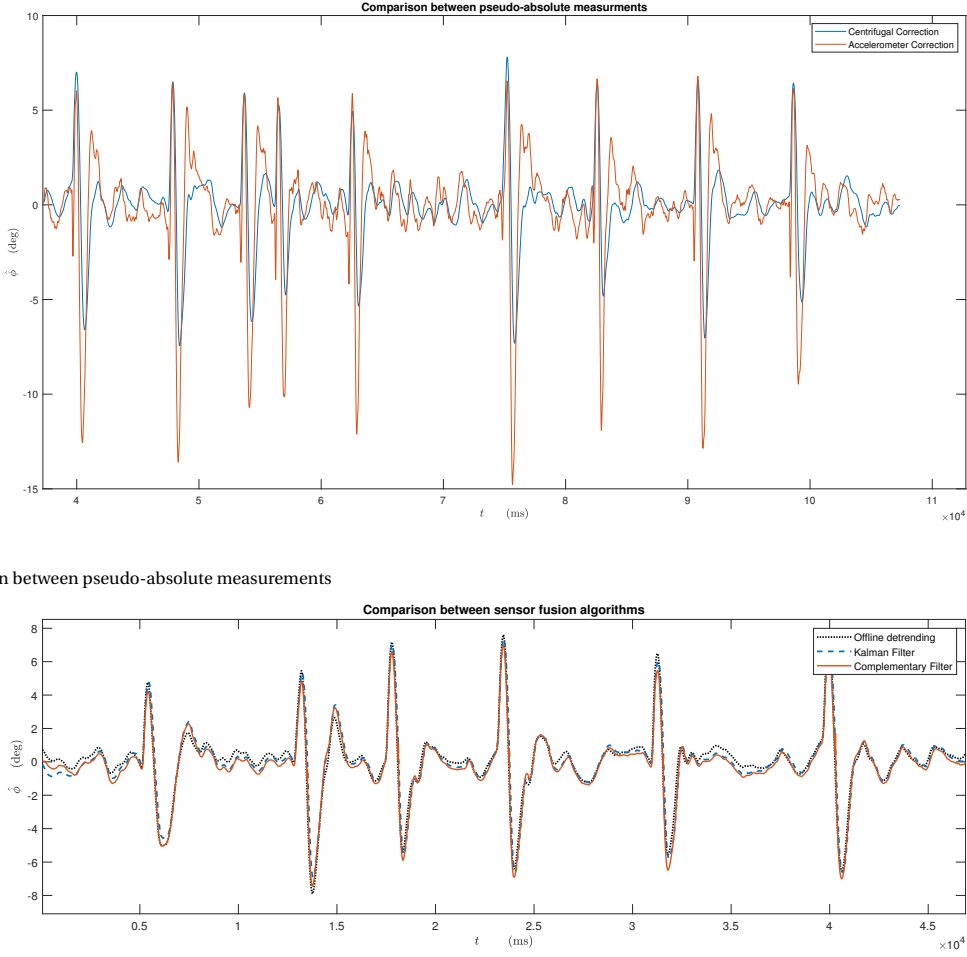
where W is the weighting function, $\hat{\phi}$ is the last available estimation of roll and $\bar{\phi}^2$ is a constant that can be used to adjust the weighting function. Sanjuro et al. used $\bar{\phi}^2 = 0.05$.

For the sensor fusion algorithm both a simple complimentary filter and a Kalman filter were tested. The complementary filter works by combining the desirable low-frequency characteristics of the absolute measurements with the desirable high-frequency characteristics of the euler integration output.

$$\hat{\phi}_k = (1 - \alpha) \cdot (\hat{\phi}_{k-1} + {}^B\omega_{x,k} \cdot dt) + \alpha \cdot \phi_m \quad (\text{B.9})$$

where k is the current iteration of the microcontroller and α is a constant, such that $0 < \alpha < 1$. The larger the α , the more pseudo absolute measurements are 'trusted'. As α goes to zero the estimate is mainly based on the integration output.

On the other hand, Kalman filters are also often used as state estimators when multiple measurement sources need to be combined into a single more reliable one. Often the output of a model is combined with absolute measurements and an estimation of the state is made by dynamically weighting the two sources of information. In this case a simple plant model is created which has $\dot{\phi} \approx {}^B\omega_x$ as input and produces the roll angle of the next time step given the previous one. In order to account for biases in the angular rate sensor an extra



(a) Comparison between pseudo-absolute measurements

(b) Comparison between sensor fusion algorithms

Figure B.1: a) Comparison between pseudo-absolute measurements. Both sources were fused with the integration output via a Kalman filter. The blue line is the result of the measurements used by Sanjurjo et al. [31] while the orange line is the result of the estimation produced using the accelerometer equation (A.3). b) Comparison between sensor fusion algorithms. For reference the output of the offline linear regression detrending is shown as a black dotted line.

state b_x is added to the model. The complete formulation is given by :

$$\begin{bmatrix} \hat{\phi} \\ \hat{b}_x \end{bmatrix}_k^- = \begin{bmatrix} 1 & -dt \\ 0 & 1 \end{bmatrix} \begin{bmatrix} \hat{\phi} \\ \hat{b}_x \end{bmatrix}_{k-1}^+ + \begin{bmatrix} dt \\ 0 \end{bmatrix} {}^B\omega_{x,k-1} \quad (\text{B.10})$$

The results are shown in figure B.1. In figure B.1a it is visible that the naive implementation using the assumption that the accelerometer only registers the gravitational acceleration does not work. However, for the first few seconds after turning on the bike the assumption is correct and a good initial condition estimate can be extracted in order to use as initial condition in the sensor fusion algorithm of choice. As far as the sensor fusion algorithm is concerned the results are shown in figure B.1b. A complimentary filter with $\alpha = 0.0022$ is used, while for the Kalman filter the process covariance matrix and measurement variance were equal to:

$$Q_P = \begin{bmatrix} 9e^{-4} & 0 \\ 0 & 3e^{-4} \end{bmatrix} dt \quad (\text{B.11})$$

$$Q_S = 0.5 \quad (\text{B.12})$$

Additionally the initial covariance matrix was equal to zero which means that the filter at the start "trusts" the model output; the Euler integration output. As a reference the result from the linear regression detrending is

also presented. The graph indicates that both methods successfully approximate the reference result. Furthermore, it is clear that with this general system model, only a slight performance gain (if any) can be gained by using the Kalman filter. Additionally, the implementation of the complimentary filter is far simpler and consequently much less computationally expensive. Had the Kalman filter been implemented on a system where an accurate dynamic model was present, the Kalman filter would – in pretty much all cases – trump the simpler complimentary filter. For this reason the complimentary filter approach was chosen for the on-line implementation of roll estimation in the steer-by-wire bicycle, considering the limiting clock speed of microcontroller Teensy 3.6.

The above pseudo-absolute measurements can only be used to estimate the roll angle. However there is a way to extract an estimation of the yaw relative to the magnetic north by using the magnetometer sensor, which is also part of the IMU. This is similar to how modern smartphones can work as a compass. Similar to how an estimation of the roll angle was made by equating the accelerometer readings with reference position where the gravitational acceleration is completley aligned with the bike's z-axis, the same can be done by equating the magnetometer readings with the reference position of the bike's x axis pointing towards the magnetic north. The magnetometer in this reference position are

$$\mathbf{B}_{ref} = B \begin{pmatrix} \cos \zeta \\ 0 \\ \sin \zeta \end{pmatrix} \quad (B.13)$$

where B is the geomagnetic field strength and ζ is the angle of inclination of the geomagnetic field measured downwards from horizontal. Both values vary over the earth's surface. Detailed geomagnetic field maps are available from the World Data Center for Geomagnetism at <http://wdc.kugi.kyoto-u.ac.jp/igrf/>. Fortunately, both B and ζ cancel out in the final formulation of the estimator.

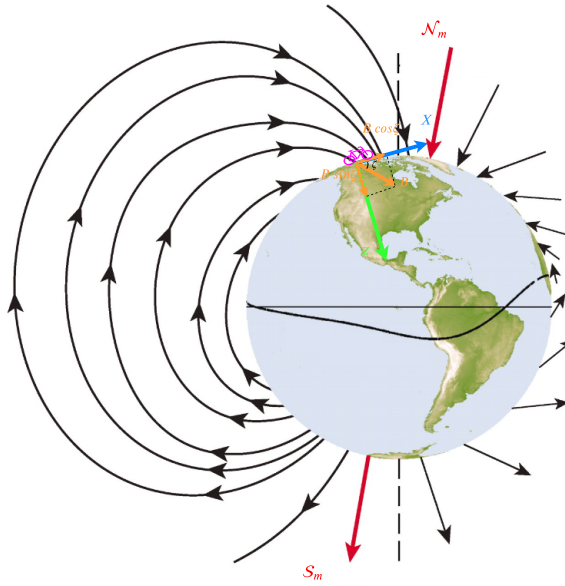


Figure B.2: Magnetic Field vectors in the reference position.

The measured magnetometer readings \mathbf{B}_p after three rotations are described by equations :

$$\mathbf{B}_p = \mathbf{R}_{xyz}(\phi, \theta, \psi) \cdot B \begin{pmatrix} \cos \zeta \\ 0 \\ \sin \zeta \end{pmatrix} + \begin{pmatrix} V_x \\ V_y \\ V_z \end{pmatrix} \quad (B.14)$$

where \mathbf{R}_{xyz} the rotation matrix defined in ??eq:rotmat2 and V_x, V_y, V_z are the components of the Hard-Iron vector, which is a fixed magnetic offset adding to the true magnetometer sensor output. The Hard-Iron offset is the sum of any intrinsic zero field offset within the magnetometer sensor itself plus permanent magnetic

fields within the PCB generated by magnetized ferromagnetic materials. It is quite normal for the Hard-Iron offset to greatly exceed the geomagnetic field. Therefore an accurate Hard-Iron estimation and subtraction are required.

The Hard-Iron offset can be estimated if we consider that the set of all 3d points defined by every magnetometer reading lies in the surface of a sphere with radius B . In the presence of the offset, the center of the sphere would be displaced by the Hard-Iron Vector \mathbf{V} . The components of vector \mathbf{V} can be estimated by fitting the magnetometer measurements to the equation:

$$(\mathbf{B}_p - \mathbf{V})^T (\mathbf{B}_p - \mathbf{V}) = B^2 \quad (\text{B.15})$$

Equation (B.15) was solved with the gradient descend method by minimizing the sum of the squared difference between the right and left hand side of the equation. The resulting Hard-Iron Offset Vecotor was :

$$\mathbf{V} = \begin{pmatrix} -22.03 & -26.14 & -1.651 \end{pmatrix} \quad [\mu\text{T}] \quad (\text{B.16})$$

In figure B.3 the locus defined by the set of vectors measured by the magnetometer is displayed. It is visible that after the correction the measurements lie on the surface of a sphere with center in the origin and radius approximately equal to 1 a.u.

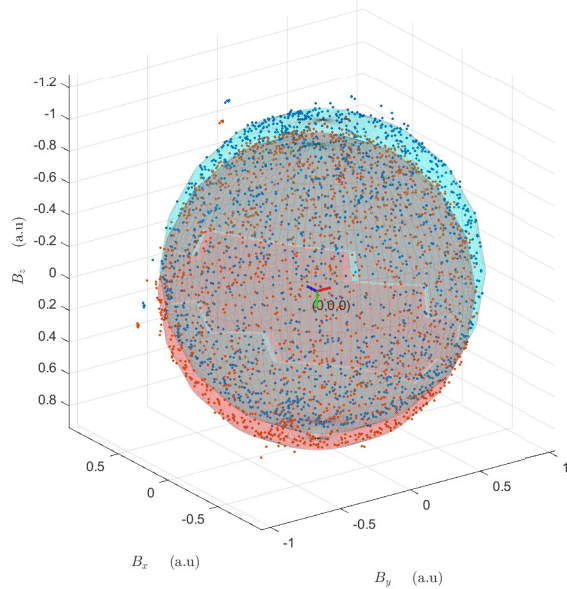


Figure B.3: The blue dots are the locus of the magnetometer readings before correcting for the hard iron offset. The red dots are the locus of the magnetometer readings after correcting for the offset. The magnetometer readings have been normalized so that 1 a.u= 49.0913 μT which is the Magnetic Field Intensity for the approximate location of TU Delft (Latitude 52° 0' 0" N and Longitude: 4° 22' 0" E).

Having estimated \mathbf{V} from equation (B.14) by assuming $\theta \approx 0$ we get :

$$\mathbf{B}_f = \mathbf{B}_p - \mathbf{V} = \mathbf{R}_x(\phi)\mathbf{R}_z(\psi) \cdot \begin{pmatrix} B \cos \zeta \\ 0 \\ B \sin \zeta \end{pmatrix} \quad (\text{B.17})$$

$$\mathbf{R}_x^T(\phi) \begin{pmatrix} B_{fx} \\ B_{fy} \\ B_{ fz} \end{pmatrix} = \begin{pmatrix} \cos \psi B \cos \delta \\ -\sin \psi B \cos \delta \\ B \sin \delta \end{pmatrix} \quad (\text{B.18})$$

$$\begin{pmatrix} B_{fx} \\ B_{fy} \cos \phi - B_{ fz} \sin \phi \\ B_{fy} \sin \phi + B_{ fz} \cos \phi \end{pmatrix} = \begin{pmatrix} \cos \psi B \cos \delta \\ -\sin \psi B \cos \delta \\ B \sin \delta \end{pmatrix} \quad (\text{B.19})$$

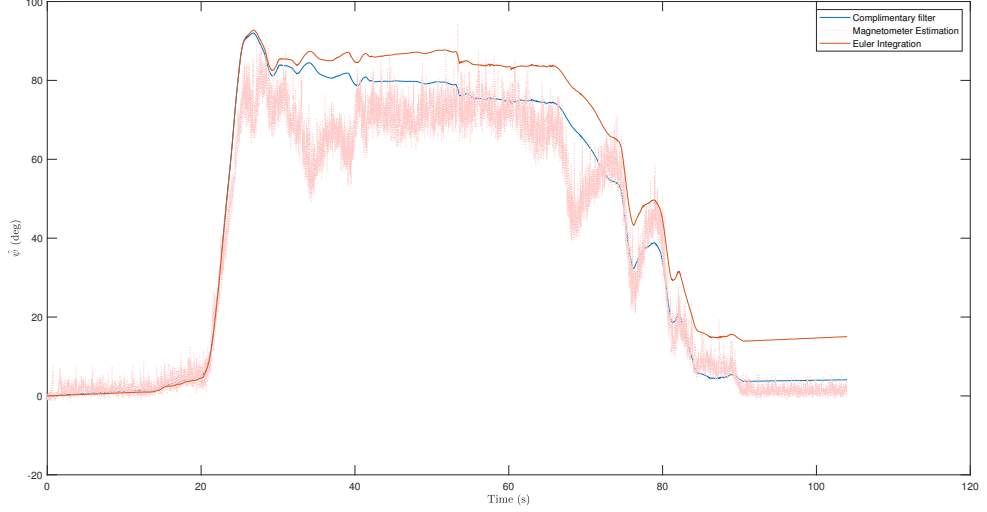


Figure B.4: Comparison of online yaw angle estimation. Red dotted line is the pure estimation from the magnetometer data. Orange line is the drifted euler integration output. Blue line is the result of the complimentary filter sensor fusing the other two signals. For the complimentary filter $a = 0.00027$.

By dividing the y and x component of equation (B.19) we get:

$$\hat{\psi} = \tan^{-1} \left(\frac{B_{fx} \sin \hat{\phi} - B_{fy} \cos \hat{\phi}}{B_{fz}} \right) \quad (\text{B.20})$$

where $\hat{\phi}$ is the estimate of roll angle obtained from the aforementioned methods. Equation (B.20) can now be used as a source of pseudo-absolute measurements for the sensor fusion algorithm of choice. Regarding signal fusion the same things apply as in the roll angle estimation case. Finally since we want the yaw angle relative to the starting position and not relative to the magnetic north the value of the first yaw estimation is subtracted from all subsequent computations.

C

ESTIMATION OF RIDER TORQUE

Given the steer rate ($\dot{\delta}$) and acceleration ($\ddot{\delta}$), moment of inertia (I_H), motor damping (b_m) and the torque applied by the handlebar motor (T_{PDH}) the equation of motion of the upper handlebar assembly can be formed (see Fig. C.1) and solved for the unknown rider input torque (T_H).

$$T_H = \ddot{\delta} I_H + \dot{\delta} b_m - T_{PDH} \quad (\text{C.1})$$

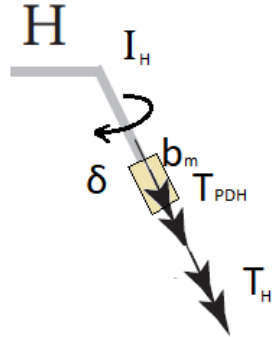


Figure C.1: Free body diagram of the upper handlebar assembly.

C.1. STEER RATE AND ACCELERATION

Since only the steering angle is directly measurable, a way needs to be found that produces accurate estimations of steer rate and steer acceleration. Simple numerical differencing techniques proved ineffective as noise effects were magnified resulting in corrupted second derivatives, even after filtering the original signal to a cutoff frequency of 10 Hz.

To combat this problem a piecewise cubic interpolation technique using the cubic spline function was used. The principle of this method is simple. Third order polynomials are fitted between the datapoints. This results in a signal that is identical to the original but instead of discrete points, it is represented by the union of polynomial functions. After this point the steer rate and acceleration can be easily obtained by taking the derivatives of the polynomials. the result of the method is seen in figure C.2.

C.2. STEERING SHAFT MOMENT OF INERTIA AND VISCOUS FRICTION

In order to make estimation of applied rider torque, the damping coefficient and the inertia of the steering shaft needs to be determined. There are multiple ways to measure inertia of complex geometries. Here an

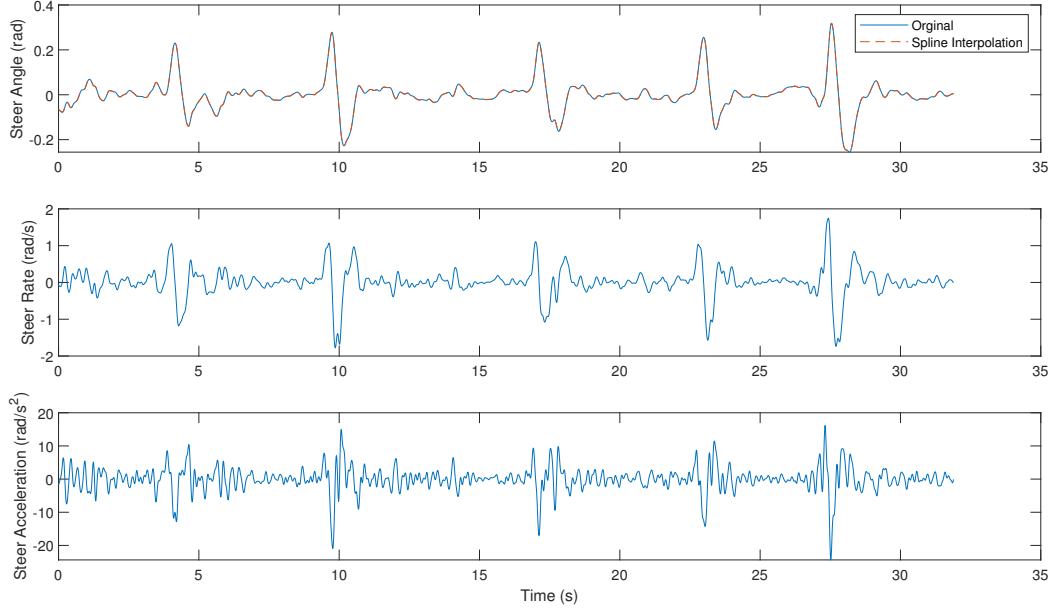


Figure C.2: Steering angle signal with its derivatives produced by the piecewise cubic spline interpolation method.

estimation through a simple experimental setup is chosen.

By connecting the steering shaft with two extension springs (see Fig.C.3) and measuring the oscillations of the steering angle δ , a mechanical system is created where it has to obey equation C.2.

$$I_H \ddot{\delta}(t) + b_m \dot{\delta}(t) + 2K\alpha^2 \delta(t) = 0 \quad (\text{C.2})$$

where K the spring elastic constant and α the moment arm shown in figure C.3.

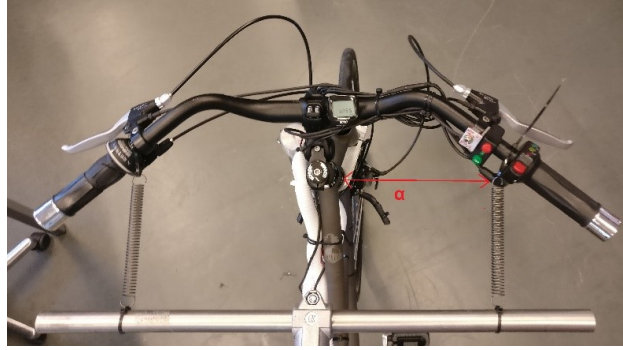


Figure C.3: Spring-handlebar assembly where α is the moment arm.

The springs ($K = 555 \text{ N/m}$ and slack length of 0.03 m) are attached to the handlebar and the system is perturbed. The measured steering angle signal from one of the perturbation tests is shown in figure C.4. The steering rate and acceleration signals are derived by the methods described in section C.1. Equation C.2 is then applied to all discrete time steps and so the system of equations C.3 is created.

$$\begin{bmatrix} \ddot{\delta}_1 & \dot{\delta}_1 \\ \ddot{\delta}_2 & \dot{\delta}_2 \\ \vdots & \vdots \\ \ddot{\delta}_N & \dot{\delta}_N \end{bmatrix} \begin{bmatrix} I_H \\ b_m \end{bmatrix} = -2K\alpha^2 \begin{bmatrix} \delta_1 \\ \vdots \\ \delta_N \end{bmatrix} \quad (\text{C.3})$$

where N the length of the recorded signal.

Since equation C.3 is linear in the parameters, the solution of the regression problem can be approximated by the use of the least squares method.

$$\begin{bmatrix} I_H \\ b_m \end{bmatrix} = -2K\alpha^2 \left(\begin{bmatrix} \ddot{\delta}_1 & \dot{\delta}_1 \\ \ddot{\delta}_2 & \dot{\delta}_2 \\ \vdots & \vdots \\ \ddot{\delta}_N & \dot{\delta}_N \end{bmatrix}^T \begin{bmatrix} \ddot{\delta}_1 & \dot{\delta}_1 \\ \ddot{\delta}_2 & \dot{\delta}_2 \\ \vdots & \vdots \\ \ddot{\delta}_N & \dot{\delta}_N \end{bmatrix} \right)^{-1} \begin{bmatrix} \ddot{\delta}_1 & \dot{\delta}_1 \\ \ddot{\delta}_2 & \dot{\delta}_2 \\ \vdots & \vdots \\ \ddot{\delta}_N & \dot{\delta}_N \end{bmatrix}^T \begin{bmatrix} \delta_1 \\ \dots \\ \delta_N \end{bmatrix} \quad (\text{C.4})$$

The system is perturbed 15 times so 15 sets of inertia and damping ratios are computed. The mean of the these was taken and resulted in $I_H = 0.0960 \text{ kg m}^2$ and $b_m = 0.2663 \text{ N s}^{-1}$

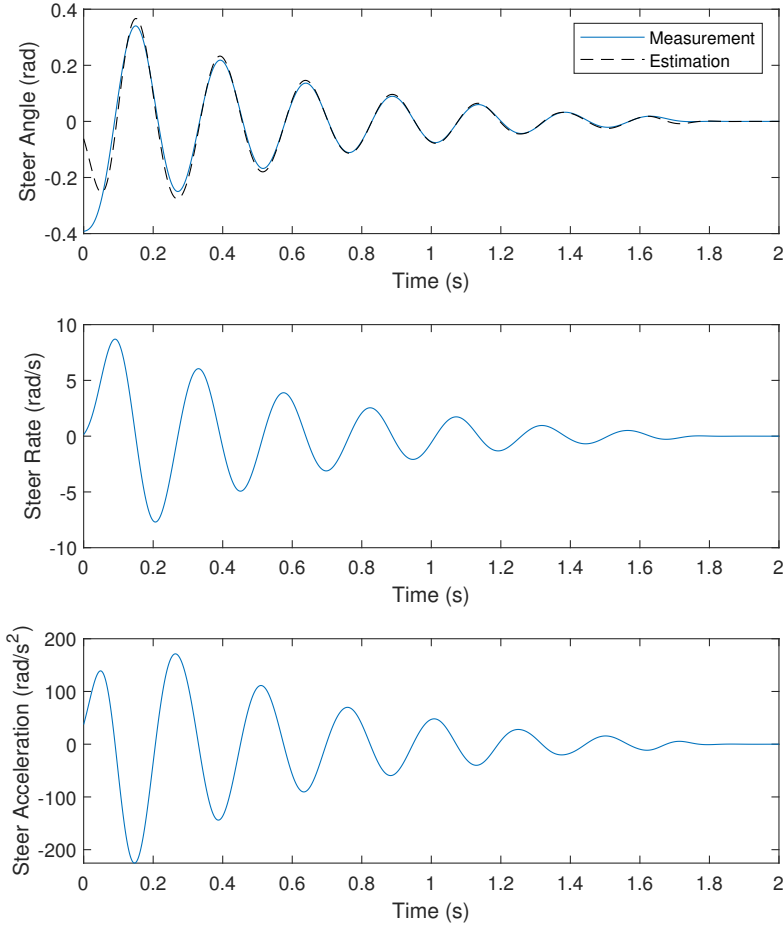


Figure C.4: Result of the first of fifteen oscillations. Blue lines indicate the measured signals while the black dotted line is the output of the model given the values of inertia and damping estimated with the least squares method.

C.3. MOTOR TORQUE INPUT VALIDATION

C.3.1. DESIGN OF TORQUE SENSOR

In order to validate that the torque exerted by the handlebar motor results in equivalent input rider torque a torque sensor is designed and attached to the steering shaft. The most common torque sensor measurement principle uses bonded strain gauge technology, where the strain gauges are bonded to a suitably designed shaft.

In the torsion of a cylindrical shaft the strain is measured by the angle of twist or angular deflection. Unfortunately stain gauges can only detect compressive and tensile strain. The strain gauges are placed with such an orientation that the shearing stress is replaced by its equivalent principal stresses. The angle and the magnitude of the principal stresses are calculated by the use of the Mohr Circle. In this case the principal tension and compressive stresses are of the same magnitude as the shearing stress and are active at an angle of 45 degrees since it is considered that no external compressive or tension force is present.

In order to design a proper cylindrical shaft for the torque sensor the diameter of the shaft is chosen such that the strain measured in the strain gauges is within the detectable range ($\epsilon_{min} = 10^{-5}$, $\epsilon_{max} = 6 \cdot 10^{-4}$). For this application, a hollow cylindrical shaft made of aluminum (AL7075 - O) is used so the unknowns are the inner and outer diameters. The strain is given in relation to the stress by Hooke's law for isotropic materials by equation (C.5). The shearing stress is in turn given by equation (C.6).

$$\epsilon = \frac{\sigma \cdot (1 + \nu)}{E} \quad (\text{C.5})$$

where ν the Poisson's ratio and E the Young's Modulus (Pa)

$$\tau = \frac{T \cdot r}{J} \quad (\text{C.6})$$

where J is the polar moment of inertia (m^4), r the distance from center to stressed surface in the given position (mm), T the twisting moment (Nm). The polar moment of inertia of a circular hollow shaft can be expressed as

$$J = \frac{\pi \cdot (D^4 - d^4)}{32} \quad (\text{C.7})$$

where d is shaft inside diameter (mm) and D is the shaft outside diameter (mm).

By inputting the above equations into a MATLAB script figure C.5 was produced. The figure was created for a fixed inner diameter of 12mm, due to limitations in the machining process. It is evident that the lower the width of the shaft the higher detection of the low level torques. For this reason a width of 2 mm was chosen. This still means that torques below 0.2Nm are not detectable. However the purpose of the torque sensor is not to provide accurate online measurements but to validate the input torques from the handlebar motor. The design of the resulting part is shown in C.6.

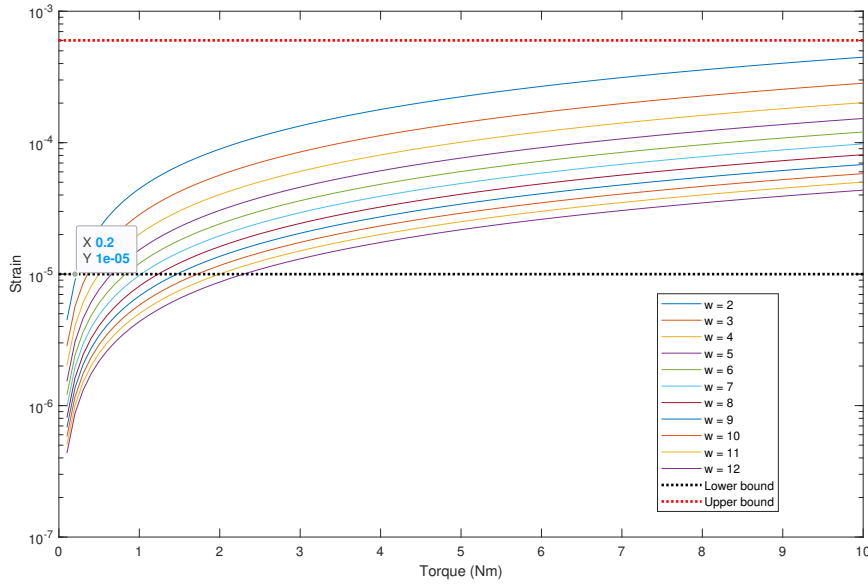


Figure C.5: Principal tensile strain in the 45 degree angle for various shaft widths (w).

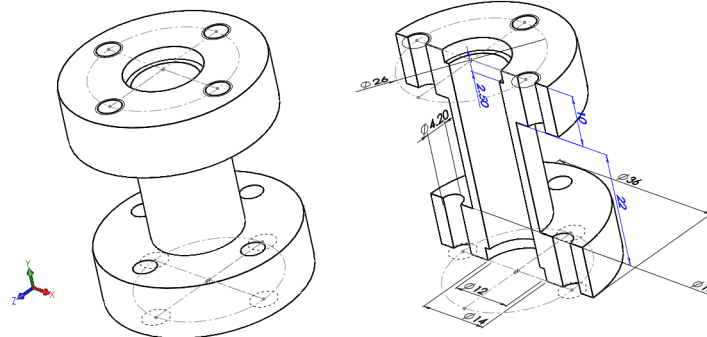


Figure C.6: Schematic of the hollow shaft.

Because it is not an ideal hollow cylinder, the shearing stress calculated analytically from the above equations needs to be validated. A static load simulation in SolidWorks is done to see how much different is the shearing stress on the external surface. As it turns out the simulation showed a shearing stress similar to the one calculated by the equations. In C.7 the simulation results for a loading of 10Nm is shown. For comparison the resulting shearing stress calculated analytically is $10.0874 \cdot 10^6 \text{N/m}^2$. For proper measurements of strain the gauge placement should gravitate towards the middle to avoid the spikes of shearing stress near the intersections between the main shaft and the cylindrical heads (see fig. C.7)

C.3.2. RESULTS

In order to validate that the commanded torque in the handlebar motor is the same as the one actually applied in the handlebar, a trial identification run was conducted to simulate steer torque levels of the experiments. The signal of the input motor torque is compared with the output of the custom made torque sensor. The results are shown in figure C.8. The mismatch of the two signals for values lower than 0.5Nm is attributed to the fact that the sensor's strain gauges cannot accurately measure the strain in the material to produce reliable output as determined analytically beforehand. Also during the measurements a slight bias of the sensor was noted when $0 < \delta < \pi/2$. Despite the aforementioned, the resulting Variance Accounted For (VAF) was

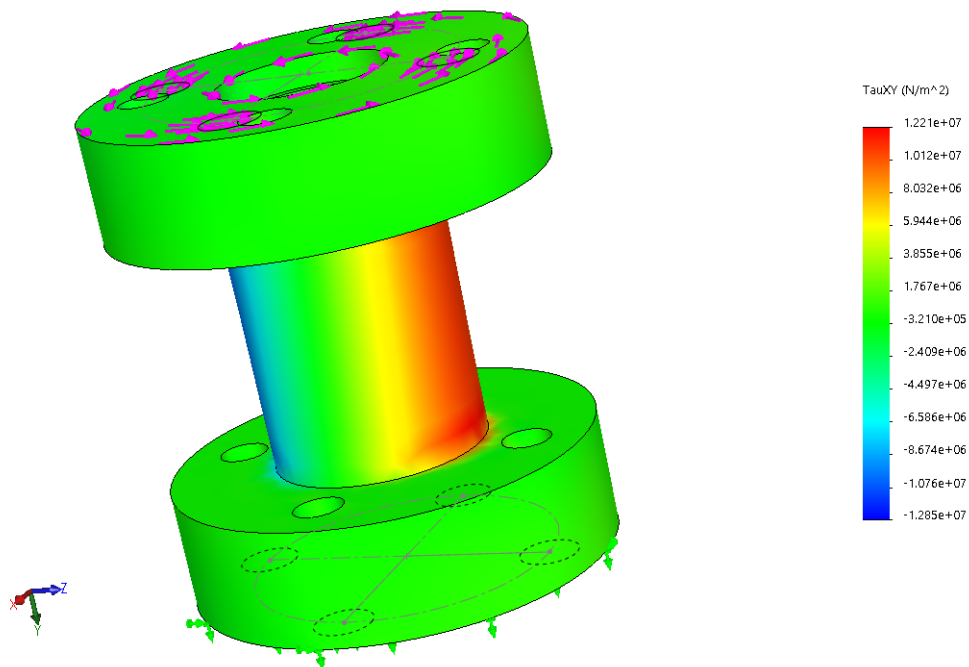


Figure C.7: Shearing stress for 10Nm loading in the axial direction.

equal to 90.77% and was deemed that the motor command torque is indeed what is being applied in the steering shaft so in all subsequent calculation it was taken as ground truth.

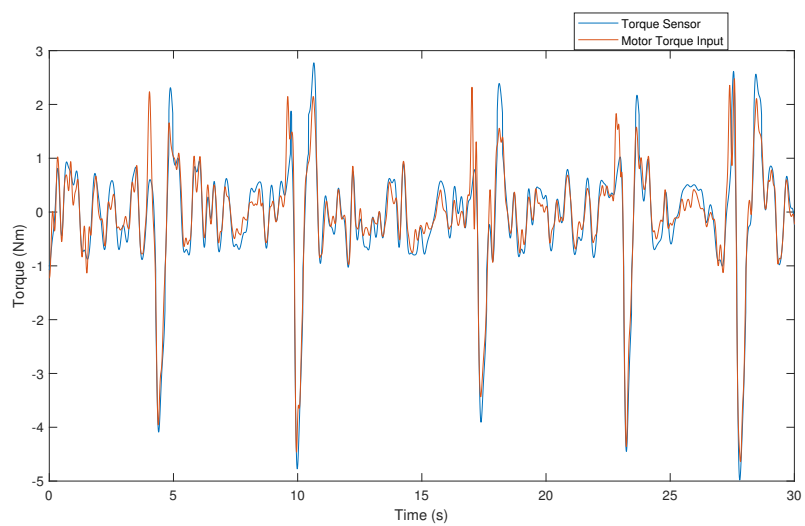


Figure C.8: Measurement of torque sensor compared to the commanded torque of the handlebar motor.

BIBLIOGRAPHY

- [1] Michael Barnett-Cowan. Vestibular perception is slow: a review. *Multisensory research*, 26(4):387–403, 2013.
- [2] European Commission. Traffic safety basic facts on cyclists. *Directorate General for Transport*, European Commission, 2018.
- [3] Laura Marchal Crespo and David J Reinkensmeyer. Haptic guidance can enhance motor learning of a steering task. *Journal of motor behavior*, 40(6):545–557, 2008.
- [4] Erwin De Vlugt, Alfred C Schouten, and Frans CT Van Der Helm. Adaptation of reflexive feedback during arm posture to different environments. *Biological cybernetics*, 87(1):10–26, 2002.
- [5] Georgios Dialynas, Christos Christoforidis, Riender Happee, and AL Schwab. The effect of haptic feedback in the balance task of bicycling. *Symposium on the Dynamics and Control of Single Track Vehicles*.
- [6] Georgios Dialynas, Riender Happee, and AL Schwab. Design and implementation of a steer-by-wire bicycle. In *Proceedings of the 7th Annual International Cycling Safety Conference*, 2018. URL <https://www.researchgate.net/publication/328808185>.
- [7] DJ Eaton. *Man-Machine Dynamics in the Stabilization of Single-Track Vehicles*, " Univ. of Michigan. PhD thesis, Ph. D. Thesis, 1975.
- [8] Johannes Edelmann, Martin Haudum, and Manfred Plöchl. Bicycle rider control modelling for path tracking. *IFAC-PapersOnLine*, 48(1):55–60, 2015. doi: 10.1016/j.ifacol.2015.05.070.
- [9] Bruce A Francis and Walter Murray Wonham. The internal model principle of control theory. *Automatica*, 12(5):457–465, 1976.
- [10] Carlos E Garcia and Manfred Morari. Internal model control. a unifying review and some new results. *Industrial & Engineering Chemistry Process Design and Development*, 21(2):308–323, 1982.
- [11] Neil H Getz. Internal equilibrium control of a bicycle. In *Proceedings of 1995 34th IEEE Conference on Decision and Control*, volume 4, pages 4285–4287. IEEE, 1995.
- [12] R Brent Gillespie, Amir H Ghasemi, and Jim Freudenberg. Human motor control and the internal model principle. *IFAC-PapersOnLine*, 49(19):114–119, 2016.
- [13] Riender Happee, Erwin De Vlugt, and Alfred C Schouten. Posture maintenance of the human upper extremity; identification of intrinsic and reflex based contributions. *SAE International Journal of Passenger Cars-Mechanical Systems*, 1(2008-01-1888):1125–1135, 2008.
- [14] Ryouhei Hayama, Sadahiro Kawahara, Shirou Nakano, and Hiromitsu Kumamoto. Resistance torque control for steer-by-wire system to improve human–machine interface. *Vehicle system dynamics*, 48(9):1065–1075, 2010.
- [15] Ronald Hess, Jason Keith Moore, and Mont Hubbard. Modeling the manually controlled bicycle. *IEEE Transactions on Systems, Man, and Cybernetics-Part A: Systems and Humans*, 42(3):545–557, 2012.
- [16] Osamu Kawakami, Yoshiki Kaneoke, Koichi Maruyama, Ryusuke Kakigi, Tomohisa Okada, Norihiro Sadato, and Yoshiharu Yonekura. Visual detection of motion speed in humans: spatiotemporal analysis by fmri and meg. *Human brain mapping*, 16(2):104–118, 2002.
- [17] JDG Kooijman and AL Schwab. A review on bicycle and motorcycle rider control with a perspective on handling qualities. *Vehicle system dynamics*, 51(11):1722–1764, 2013.

- [18] JDG Kooijman, Jacob Philippus Meijaard, Jim M Papadopoulos, Andy Ruina, and AL Schwab. A bicycle can be self-stable without gyroscopic or caster effects. *Science*, 332(6027):339–342, 2011.
- [19] I. Krul, S. Nijman, and C. Stam. Verkeersongevallen 2016, 2016. URL <https://www veiligheid nl/organisatie/over-veiligheidnl/publicaties>.
- [20] Y Marumo and M Nagai. Steering control of motorcycles using steer-by-wire system. *Vehicle System Dynamics*, 45(5):445–458, 2007.
- [21] Yoshitaka Marumo and Nozomi Katagiri. Control effects of steer-by-wire system for motorcycles on lane-keeping performance. *Vehicle System Dynamics*, 49(8):1283–1298, 2011.
- [22] Duane T McRuer and Ezra S Krendel. The human operator as a servo system element. *Journal of the Franklin Institute*, 267(5):381–403, 1959.
- [23] Duane T McRuer, Dunstan Graham, and Ezra S Krendel. Manual control of single-loop systems: Part i. *Journal of the Franklin Institute*, 283(1):1–29, 1967.
- [24] Duane T McRuer, Dunstan Graham, and Ezra S Krendel. Manual control of single-loop systems: Part ii. *Journal of the Franklin Institute*, 283(2):145–168, 1967.
- [25] Jaap P Meijaard, Jim M Papadopoulos, Andy Ruina, and Arend L Schwab. Linearized dynamics equations for the balance and steer of a bicycle: a benchmark and review. *Proceedings of the Royal society A: mathematical, physical and engineering sciences*, 463(2084):1955–1982, 2007.
- [26] RC Miall, D Jo Weir, Daniel M Wolpert, and JF Stein. Is the cerebellum a smith predictor? *Journal of motor behavior*, 25(3):203–216, 1993.
- [27] Jason K Moore, JDG Kooijman, AL Schwab, and Mont Hubbard. Rider motion identification during normal bicycling by means of principal component analysis. *Multibody System Dynamics*, 25(2):225–244, 2011.
- [28] Jason Keith Moore. *Human control of a bicycle*. University of California, Davis Davis, CA, 2012.
- [29] R Douglas Roland. Computer simulation of bicycle dynamics. In *Proceedings of the ASME Symposium Mechanics and Sport*, pages 35–83, 1973.
- [30] R Douglas Roland Jr and E Daniel. Massing. a digital computer simulation of bicycle dynamics. Technical report, Calspan Report YA-3063-K-1, Cornell Aeronautical Laboratory, Inc., Buffalo . . . , 1971.
- [31] Emilio Sanjurjo, Miguel A Naya, Javier Cuadrado, and Arend L Schwab. Roll angle estimator based on angular rate measurements for bicycles. *Vehicle System Dynamics*, pages 1–15, 2018.
- [32] Emilio Sanjurjo, Miguel A Naya, Javier Cuadrado, and Arend L Schwab. Roll angle estimator based on angular rate measurements for bicycles. *Vehicle System Dynamics*, 57(11):1705–1719, 2019.
- [33] Al Schwab, Pdl De Lange, R Happee, and Jason K Moore. Rider control identification in bicycling using lateral force perturbation tests. *Proceedings of the Institution of Mechanical Engineers, Part K: Journal of Multi-body Dynamics*, 227(4):390–406, 2013. doi: 10.1177/1464419313492317.
- [34] Robin S Sharp. The stability and control of motorcycles. *Journal of mechanical engineering science*, 13(5):316–329, 1971.
- [35] OJM Smith. Closed control of loops with dead time. *Chemical Engineering Progress*, 53:217–219, 1957.
- [36] Frans CT Van der Helm, Alfred C Schouten, Erwin de Vlugt, and Guido G Brouwn. Identification of intrinsic and reflexive components of human arm dynamics during postural control. *Journal of neuroscience methods*, 119(1):1–14, 2002.
- [37] Herman van der Kooij, Ron Jacobs, Bart Koopman, and Frans van der Helm. An adaptive model of sensory integration in a dynamic environment applied to human stance control. *Biological cybernetics*, 84(2):103–115, 2001.

- [38] A Van Lunteren, HG Stassen, and MSH Schlemper. On the influence of drugs on the behavior of a bicycle rider. In *Proceedings of the 6th Annual Conference on Manual Control, Wright Patterson AFB, OH, USA*, pages 7–9, 1970.
- [39] Sarah Catherine Walpole, David Prieto-Merino, Phil Edwards, John Cleland, Gretchen Stevens, and Ian Roberts. The weight of nations: an estimation of adult human biomass. *BMC public health*, 12(1):439, 2012.
- [40] David H Weir. A manual control view of motorcycle handling. Technical report, 1973.
- [41] Daniel M Wolpert, Zoubin Ghahramani, and Michael I Jordan. An internal model for sensorimotor integration. *Science*, 269(5232):1880–1882, 1995.